Mechanics of Materials 168 (2022) 104293

Contents lists available at ScienceDirect

Mechanics of Materials

journal homepage: www.elsevier.com/locate/mechmat

Experimental characterization and crystal plasticity modeling of dual-phase steels subjected to strain path reversals

Sowmya Daroju [a], Toshihiko Kuwabara [b], Marko Knezevic [a,*]

[a] Department of Mechanical Engineering, University of New Hampshire, Durham, NH, 03824, USA
[b] Division of Advanced Mechanical Systems Engineering, Institute of Engineering, Tokyo University of Agriculture and Technology, Tokyo, 184-8588, Japan

ARTICLE INFO

Keywords:
Microstructures
Cyclic loading
Backstress fields
Crystal plasticity
Dual-phase steels

ABSTRACT

This paper is concerned with monotonic and load reversal deformation of four dual-phase (DP) 590, 780, 980, 1180 and one martensitic (MS) 1700 steel sheets. While the monotonic data are presented for all steels, the load reversal data are provided for DP 590, DP 780, and DP 1180. Particularities pertaining to the reversal deformation including the decreasing hardening rate during forward tension, a linear and then a non-linear unloading, followed by the Bauschinger effect, and a shift in the hardening rate during continuous straining were quantified and discussed as a function of loading history. Moreover, parameters such as the reloading stress differential, reloading softening stress, ratcheting strain, and unloading deviation stress were determined and discussed as a function of martensite fraction. The data were interpreted and predicted using an elasto-plastic self-consistent (EPSC) crystal plasticity model incorporating anisotropic elasticity, a dislocation density based hardening law, and a slip system backstress law. The model parameters associated with the slip strengths of ferrite and martensite and backstress were established. This work demonstrated the ability of crystal plasticity modeling to account for the co-dependent nature of crystallographic slip in ferrite and martensite and the sources of hardening caused by history-dependent dislocation density evolution and backstress to predict not only monotonic but also hysteresis in plastic response during the forward-reversal cycles. The combination of comprehensive experimental data and modeling results allowed us to infer that the tradeoff between the magnitude of backstress per phase and the volume fraction of ferrite versus martensite per steel governs the unloading and subsequent yielding per steel, while the dissolution of dislocations facilitates capturing the hardening rates during load reversal deformation.

1. Introduction

Strain applied in the opposite direction with respect to that applied during prior straining gives rise to the load reversal deformation path. Such deformation path changes are often exerted on the material in metal forming processes (Hosford and Caddell, 1993). Upon the load reversal, the material first exhibits linear unloading, which is followed by non-linear unloading (Barrett and Knezevic, 2020; Cullen and Korkolis, 2013; Ghorbanpour et al., 2017; Roemer et al., 2019; Wagoner et al., 2013; Yoshida et al., 2002). Next, the yield stress changes relative to that achieved at the end of prior straining. The phenomenon is referred to as the Bauschinger effect (BE) (Bauschinger, 1886). With continuous straining in the reverse direction, the hardening rate is usually smaller than that observed during prior straining. The phenomenon is referred to as the permanent softening (Hasegawa et al., 1975; Zang et al., 2013). The phenomena pertaining to the deformation involving load reversals are driven by plasticity induced microstructural evolution, as summarized below.

The first phenomenon upon load reversal is the unloading of a strained material (Deng et al., 2015; Jahedi et al., 2014; Pavlina et al., 2015; Sritharan and Chandel, 1997; Yoshida et al., 2002). The origin of the nonlinear portion of unloading is a re-emission of dislocations piled-up at grain and phase boundaries during forward straining (Mompiou et al., 2012; Sritharan and Chandel, 1997). The re-emission of these loosely-tangled dislocations in pile-ups is accompanied by the relaxation of micro-backstress fields emanating from the pile-ups (Sritharan and Chandel, 1997). During stress relaxation, these mobilized dislocations from the pile-ups quickly vanish contributing to an increase

* Corresponding author. University of New Hampshire, Department of Mechanical Engineering, 33 Academic Way, Kingsbury Hall, W119, Durham, NH, 03824, USA.
E-mail address: marko.knezevic@unh.edu (M. Knezevic).

https://doi.org/10.1016/j.mechmat.2022.104293
Received 26 September 2021; Received in revised form 12 March 2022; Accepted 18 March 2022
Available online 19 March 2022

in the forest dislocation density causing strain hardening (Dotsenko, 1979; Kruml et al., 2008; Mohebbi et al., 2015).

The second phenomenon proceeding after the unloading is the BE. The primary origin of BE pertains to intra-granular backstress sources of incompatibilities between hard regions (e.g. dislocation cell walls) and soft regions (e.g. cell interiors) (Demir and Raabe, 2010; Gough et al., 1927; Kassner et al., 2013; Mughrabi, 1983). The secondary origin of BE pertains to inter-granular backstress sources that develop due to the anisotropy between grains of different crystal orientation (Abel, 1987; Nieh and Nix, 1986; Stout and Rollett, 1990; Verma et al., 2011). Here, a softer grain surrounded by harder grains will undergo greater plastic deformation than the surrounding neighbors. Such incompatibilities in accommodating plastic strain cause the plastic strain gradients in the microstructure. The dislocations building up the gradients are referred to as the geometrically necessary dislocations (GNDs) (Bayley et al., 2006; Fleck et al., 1994). These long range internal stresses whether intra-granular or inter-granular acts against the applied loading. Upon the reversal of the loading direction, the backstress fields combine with the applied loading inducing a drop in the yield stress. Orowan's theory justifies the BE in crystals based on the reduction in the resistance to dislocation glide in the reverse motion from that during prior forward straining (Orowan, 1959). The reverse path is easier because any obstacles on the forward path have been overcome. The strain incompatibilities are greater in multi-phase materials between grains of different phases than in single-phase materials between grains of the same phase because of a larger strength differential between phases than between grains in the same phase. As a result, the backstress fields govern a greater portion of the local and overall mechanical behavior in multi-phase materials than in single-phase materials (Brown and Stobbs, 1971; Kadkhodapour et al., 2011; Nesterova et al., 2015; Taupin et al., 2013).

The third phenomenon following re-yielding is the permanent softening. The underlying cause of the phenomenon is a competition between the annihilation/dissolution of existing dislocations and buildup of new dislocations during deformation in the reverse direction (Kitayama et al., 2013; Stout and Rollett, 1990; Wilson et al., 1990). The effect is more pronounced in multi-phase materials (Bate and Wilson, 1986; Gardey et al., 2005; Hasegawa et al., 1975; Wilson and Bate, 1986).

Modeling of forming processes involving load reversals requires material models capable of capturing the above summarized phenomena (Li et al., 2002; Sharma et al., 2021). A range of macroscopic plasticity models combining isotropic and kinematic hardening laws attempting to represent the above summarized deformation physics have been developed (Armstrong and Frederick, 1966; Chaboche and Rousselier, 1983; Chaboche, 1977, 2008; Hu et al., 1992; Jahedi et al., 2015b; McDowell, 1992). These models, while computationally efficient and suitable to couple with the finite element method (FEM) codes, do not account for microstructural evolution and underlying dislocation processes and sources of backstress fields. Moreover, these models contain a large number of adjustable parameters whose identification is involved and often demands a set of complex mechanical tests (Feng et al., 2020; Smith et al., 2014). Since not microstructure sensitive, these models represent a specific material state and are best applicable to the loading conditions used in the model adjusting process.

Models based on crystal plasticity theory provide more flexibility to incorporate physics of deformation because these models consider crystallography of deformation mechanisms and can capture microstructural evolution and underlying elasto-plastic anisotropy. Besides, these models are not restricted to a given state of the material or a specific loading condition, and therefore are more robust and predictive than macroscopic plasticity models. A number of crystal plasticity models have been developed in the course of last few decades ranging from Taylor-type upper-bound models (Fromm et al., 2009; Knezevic et al., 2008, 2009; Knezevic and Kalidindi, 2007, 2017; Knezevic and Savage, 2014; Savage and Knezevic, 2015; Taylor, 1938), mean-field self-consistent (SC) models (Knezevic et al., 2013a, 2014b, 2016; Lebensohn and Tomé, 1993; Lentz et al., 2015a, 2015b; Risse et al., 2017; Turner and Tomé, 1994; Zecevic and Knezevic, 2018a) to spatially resolved techniques such as crystal plasticity finite element (Ardeljan and Knezevic, 2018; Ardeljan et al., 2015, 2016b; Barrett et al., 2018; Feather et al., 2020; Jahedi et al., 2015a, 2017b; Kalidindi et al., 1992; Knezevic et al., 2010, 2014a) and Green's function fast Fourier transform formulations (Eghtesad et al., 2018a, 2018c; Lebensohn et al., 2012Eghtesad and Knezevic, 2021a, 2021b). While the spatial models can be used for more detailed simulations accounting for grain-to-grain interactions, the Taylor-type and SC models are more computationally efficient and have proven effective in predicting the overall flow stress and evolution of texture in polycrystalline metals. Additionally, these models can serve as constitutive laws in the FEM modeling and simulations (Barrett and Knezevic, 2019; Barrett et al., 2020; Knezevic et al., 2013b; Segurado et al., 2012; Zecevic et al., 2016a, 2017a; Zecevic and Knezevic, 2017, 2019). In such formulations, the spatial variations in deformation from point to point across the FEM model relax the particular homogenization assumptions (Ardeljan et al., 2016a; Feather et al., 2019; Feather et al., 2021; Savage et al., 2018; Savage et al., 2021b; Zecevic and Knezevic, 2018b; Zecevic et al., 2015a, b).

A crystallography-based elasto-plastic self-consistent (EPSC) model featuring a dislocation-based hardening law and accounting for inter-granular stress fields and intra-granular backstress sources at the slip system level has been used to interpret the load reversal deformation of DP 590 (Zecevic et al., 2016b). The model has also been successfully adjusted to model the elastic anisotropy of DP 590, DP 980, DP 1180, and MS 1700 steels (Cantara et al., 2019; Eghtesad and Knezevic, 2020; Jahedi et al., 2015c). Modeling elastic deformation is essential in predicting the material response under non-proportional loading and, especially, under unloading of pre-strained material. Predicting the elastic unloading is critical for more accurate prediction of the residual stress amongst grains or phases. The earlier works also determined fraction of martensite versus ferrite in these steels (Poulin et al., 2020; Zecevic et al., 2016b). Combining these modeling and characterization advances, the present work measures and models the monotonic response of DP 590, DP 780, DP 980, DP 1180, and MS 1700 and the cyclic tension-compression response to large strains of DP 590, DP 780, and DP 1180 steels. The large body of mechanical data for DP steel sheets is presented and used to calibrate and validate the model. To initialize the model, neutron diffraction measurements of texture were performed. The fitting parameters of the model are calibrated for ferrite and martensite using partial data. Based on the predictions of the remaining data, the model is regarded as capable of modeling the elasto-plastic monotonic pre-loading to various strain levels followed by hysteresis in the plastic regime with multiple forward-reversal cycles of the steels using a single set of fitting parameters per phase. In particular, the monotonic hardening, the non-linear unloading, the BE, and the changes in the hardening rates during strain reversals are predicted for every steel. The data, calculations, and insights pertaining to the deformation behavior of the steels are presented and discussed in the paper.

2. Materials and experiments

The materials investigated in this work are DP advanced high strength steel (AHSS) sheets of DP 590, DP 780, DP 980, DP 1180, and one martensitic steel sheet, MS 1700. The sheets were acquired from the United States Steel Corporation (US Steel). DP 590, DP 780, and DP 980 underwent the hot dip (HD) processing line, while DP1180 underwent the continuous annealing line (CAL). DP 590 and DP 780 were galvannealed (HDGA) coated. DP 980 was galvanized (HDGI) coated. DP 1180 and MS 1700 were bare. Chemical composition of the DP steels (wt%) is provided in Table 1. The thicknesses of the sheets were 1.3 mm, 1.4 mm, 1 mm, 1 mm, and 1 mm for DP 590, DP 780, DP 980, DP 1180, and MS 1700, respectively. These steel sheets are typically used for auto-body

Table 1
Chemical composition of DP steels (wt%).

	C	Mn	P	S	Si	Cu	Ni	Cr	Mo
DP 590	0.073	1.97	0.014	0.006	0.017	0.04	0.01	0.2	0.172
DP 780	0.1	2.163	0.015	0.006	0.014	0.03	0.01	0.26	0.332
DP 980	0.11	2.411	0.013	0.005	0.013	0.027	0.009	0.255	0.385
DP 1180	0.168	2.222	0.015	0.0053	1.421	0.021	0.007	0.036	0.013

	Sn	Al	Zr	V	Cb	Ti	B	N_2
DP590	0.002	0.045		0.001			0.0001	0.005
DP780	0.003	0.048		0.001	0.003	0.001	0.0001	0.006
DP980	0.006	0.049	0.005	0.011	0.004	0.002	0.0001	0.0033
DP1180	0.007	0.051	0.005	0.012	0.007	0.039	0.0004	0.0086

and structure applications.

The studied steels offer a compromise between strength and ductility as a result of their underlying microstructure that consists of a softer ferritic phase and a harder martensitic phase. While the former phase provides ductility, the latter phase provides the strengthening. Electron backscatter diffraction (EBSD) and secondary electrons (SE) imaging was performed in earlier work to characterize grain structure and phase fractions (Poulin et al., 2020). Volume fraction of martensite for the studied steels is given in Table 2.

The tradeoff between strength and ductility of these steels is governed by the volume fraction of these two phases (Calcagnotto et al., 2012; Ghaei et al., 2015; Gong et al., 2016; Kudzal et al., 2020; Ma et al., 2016; Woo et al., 2012; Zecevic et al., 2019b). Further improvements are possible by phase distribution (Bhargava et al., 2018; Calcagnotto et al., 2011). The secondary effects influencing the behavior of these steels are due to grain size and crystallographic texture per phase. Local grain-level plasticity in these steels is highly inhomogeneous due to the contrasting characteristics of the constituent phases. For example, larger grains suitably oriented for slip deform plastically earlier than smaller grains of ferrite (Tasan et al., 2014). Additionally, plastic strain can localize in channels of ferrite between martensite regions as well as at martensite/ferrite phase interfaces (Kapp et al., 2011; Tasan et al., 2014; Woo et al., 2012; Yaddanapudi et al., 2021). Such localizations limit formability in sheet metal forming operations (Bhadeshia, 2002; Nikhare et al., 2011; Saeidi et al., 2015; Shi and Gelisse, 2006; Wagoner et al., 2009; Xue et al., 2016).

To evaluate the behavior of the steels in large strain cyclic tension-compression, experiments were performed relying on the testing setup and procedure developed in the earlier works (Kuwabara et al., 2001, 2009; Verma et al., 2011). We only indicate that the strain was measured using a YFLA-2 (Tokyo Sokki Kenkyujo) high-elongation strain-gages. Additionally, tensile tests were performed according to the ASTM E−8 standard on an MTS Landmark 370 servo-hydraulic testing machine. During these experiments, the strain was measured using the VIC-2D Digital Image Correlation (DIC) system. The DIC strain measurements were validated with those of a mechanical extensometer. A nominal strain rate of 5×10^{-4}/s was used for all tests. All tests were performed at room temperature.

3. Material model

The EPSC model was originally developed in (Turner and Tomé, 1994), while the particular version from (Zecevic et al., 2016b) is used here to interpret the load reversal deformation of DP steels. The model treats a polycrystal as a collection of ellipsoidal grains with a specific crystallographic orientation and a volume fraction. Overall properties of the polycrystal are obtained using the SC homogenization scheme in which each grain is considered as an elasto-plastic inclusion in the homogeneous-equivalent-medium (HEM). The properties of the HEM are those sought properties of the polycrystal. In the model description that follows, we use "·" notation for a contracted (dot) product and "$\otimes$" notation for an uncontracted (tensor) product.

Table 2
Volume fraction of martensite for the studied steels.

DP 590	DP 780	DP 980	DP 1180	MS 1700
7.7%	34%	39%	45%	85%

The strain rate and Jaumann stress rate at the polycrystal level are linked using a linear relationship

$$\widehat{\boldsymbol{\sigma}} = \mathbf{L}\dot{\boldsymbol{\varepsilon}} \tag{1}$$

with $\mathbf{L}$ denoting the instantaneous elasto-plastic stiffness tensor of the overall polycrystal. The solution for $\mathbf{L}$ is obtained iteratively using the standard SC procedure (Turner and Tomé, 1994), which ensured the stress equilibrium and strain compatibility (Eshelby, 1957). A strain rate at the grain-level and that at the overall polycrystal-level are related using

$$\dot{\boldsymbol{\varepsilon}}^c = \mathbf{A}^c\dot{\boldsymbol{\varepsilon}} \tag{2}$$

where $\mathbf{A}^c = (\mathbf{L}^c + \mathbf{L}^{c^*})^{-1}(\mathbf{L}^{c^*} + \mathbf{L})$ is the localization tensor based on $\mathbf{L}^c$, which is the instantaneous crystal, c, elasto-plastic stiffness tensor and $\mathbf{L}^{c^*} = \mathbf{L}(\mathbf{S}^{c-1} - \mathbf{I})$ is the effective stiffness tensor. The effective stiffness relates the stress and strain rate deviations between grains and HEM as $(\widehat{\boldsymbol{\sigma}}^c - \widehat{\boldsymbol{\sigma}}) = -\mathbf{L}^{c^*}(\dot{\boldsymbol{\varepsilon}}^c - \dot{\boldsymbol{\varepsilon}})$. $\mathbf{S}^c$ is the symmetric portion of the Eshelby tensor and $\mathbf{I}$ is the fourth rank identity. The polycrystal stress and strain rate are the volume average of the corresponding quantities at the grain-level

$$\widehat{\boldsymbol{\sigma}} = \langle\widehat{\boldsymbol{\sigma}}^c\rangle \tag{3}$$

and

$$\dot{\boldsymbol{\varepsilon}} = \langle\dot{\boldsymbol{\varepsilon}}^c\rangle \tag{4}$$

The expression for $\mathbf{L}$ is then

$$\mathbf{L} = \langle\mathbf{L}^c\mathbf{A}^c\rangle\langle\mathbf{A}^c\rangle^{-1} \tag{5}$$

Given the Jaumann stress rate, the Cauchy stress rate is $\dot{\boldsymbol{\sigma}} = \widehat{\boldsymbol{\sigma}} + \langle\mathbf{W}^c\boldsymbol{\sigma}^c\rangle - \langle\boldsymbol{\sigma}^c\mathbf{W}^c\rangle = \mathbf{L}\dot{\boldsymbol{\varepsilon}} + \langle\mathbf{W}^c\boldsymbol{\sigma}^c\rangle - \langle\boldsymbol{\sigma}^c\mathbf{W}^c\rangle$, where $\mathbf{W}^c$ is the lattice spin tensor of a crystal, c.

The constitutive relation at the grain-level is

$$\widehat{\boldsymbol{\sigma}}^c = \mathbf{C}^c\left(\dot{\boldsymbol{\varepsilon}}^c - \sum_s \mathbf{m}^{c,s}\dot{\gamma}^{c,s}\right) - \boldsymbol{\sigma}^c tr(\dot{\boldsymbol{\varepsilon}}^c) \tag{6}$$

with $\mathbf{C}^c$ as the grain-level elastic stiffness tensor calculated based on the single crystal elastic constants established in (Cantara et al., 2019) and $\sum_s \mathbf{m}^{c,s}\dot{\gamma}^{c,s}$ as the plastic strain rate expressed as the sum over the slip system, s, shear strain rates, $\dot{\gamma}^{c,s}$. Here, $\mathbf{m}^{c,s} = 0.5(\mathbf{b}^{c,s}\otimes\mathbf{n}^{c,s} + \mathbf{n}^{c,s}\otimes\mathbf{b}^{c,s})$ is the symmetric part of the Schmid tensor with $\mathbf{b}^{c,s}$ and $\mathbf{n}^{c,s}$ are unite vectors representing the slip system direction and slip system plane normal, respectively. Like at the polycrystal level, the linear relationship between the grain strain rate and Jaumann stress rate is

$$\widehat{\boldsymbol{\sigma}}^{c} = \mathbf{L}^{c}\dot{\boldsymbol{\varepsilon}}^{c} \tag{7}$$

where $\mathbf{L}^{c}$ is:

$$\mathbf{L}^{c} = \mathbf{C}^{c} - \mathbf{C}^{c}\sum_{s}\mathbf{m}^{c,s}\otimes\left(\sum_{s'}(X^{ss'})^{-1}\mathbf{m}^{c,s'}(\mathbf{C}^{c}-\boldsymbol{\sigma}^{c}\otimes\mathbf{i})\right) - \boldsymbol{\sigma}^{c}\otimes\mathbf{i} \tag{8}$$

with:

$$X^{ss'} = h^{ss'} + h_{bs}^{ss'} + \mathbf{C}^{c}\cdot\mathbf{m}^{c,s}\otimes\mathbf{m}^{c,s'} \tag{9}$$

To activate a slip system in EPSC, $\mathbf{m}^{c,s}\cdot\boldsymbol{\sigma}^{c} - \tau_{bs}^{c,s} = \tau_{c}^{c,s}$ and $\mathbf{m}^{c,s}\cdot\ \widehat{\boldsymbol{\sigma}}^{c} - \dot{\tau}_{bs}^{c,s} = \dot{\tau}_{c}^{c,s}$ conditions need to be satisfied. In the first condition, the resolved shear stress corrected for the backstress, $\tau_{bs}^{c,s}$, approaches the value of slip resistance, $\tau_{c}^{c,s}$, while in the second condition, the stress is enforced to remain on the crystal yield surface evolving with hardening. The slip resistance, $\dot{\tau}_{c}^{c,s}$, and backstress, $\dot{\tau}_{bs}^{c,s}$, rates are linked with shearing rates, $\dot{\gamma}^{c,s}$, using (Zecevic and Knezevic, 2015):

$$\dot{\tau}_{c}^{c,s} = \sum_{s'}h^{ss'}\dot{\gamma}^{c,s'} \tag{10}$$

$$\dot{\tau}_{bs}^{c,s} = \sum_{s'}h_{bs}^{ss'}\dot{\gamma}^{c,s'} \tag{11}$$

with $h^{ss'}$ and $h_{bs}^{ss'}$ being the hardening and the backstress matrices, respectively. Expressions for $h^{ss'}$ and $h_{bs}^{ss'}$ can readily be derived from the hardening and backstress evolution laws, which will be described below.

In order to calculate the reorientation of crystal orientations in both ferrite and martensite grains, the lattice spin tensor, $\mathbf{W}^{c}$, is used and calculates using

$$\mathbf{W}^{c} = \mathbf{W}^{app} + \boldsymbol{\Pi}^{c} - \mathbf{W}^{p,c} \tag{17}$$

with $\mathbf{W}^{app}$ as the applied rotation rate, $\boldsymbol{\Pi}^{c}$ as the antisymmetric part of the Eshelby tensor (Lebensohn and Tomé, 1993), and $\mathbf{W}^{p,c}$ as the plastic spin, which is obtained from the shearing rates

$$\mathbf{W}^{p,c} = \sum_{s}\mathbf{q}^{c,s}\dot{\gamma}^{c,s} \tag{18}$$

with $\mathbf{q}^{c,s} = 0.5(\mathbf{b}^{c,s}\otimes\mathbf{n}^{c,s} - \mathbf{n}^{c,s}\otimes\mathbf{b}^{c,s})$.

3.1. Hardening law

In the description below, the superscript α denotes slip modes i.e. $\alpha = 1$ for $\{110\}\langle 1\bar{1}1\rangle$ and $\alpha = 2$ for $\{112\}\langle 11\bar{1}\rangle$, whereas the superscripts s and s' denote the individual slip systems in the modes. Note that the slip systems in EPSC have positive $s+$ and negative s-directions i.e. have the same slip plane but opposite directions.

The slip resistance evolves from an initial value, τ_{0}^{α}, that includes the Peierls stress, the barrier grain size contribution, and the initial content of dislocations contribution per slip system based on the thermally activated rate of dislocation storage

$$\tau_{c}^{s} = \tau_{0}^{\alpha} + \tau_{forest}^{s} + \tau_{deb}^{\alpha} \tag{19}$$

where, τ_{forest}^{s} is a forest dislocations term and τ_{deb}^{α} is a debris dislocations term. The former term is modeled using the Taylor-type relation (Kitayama et al., 2013; Knezevic et al., 2012; Taylor, 1992)

$$\tau_{for}^{s} = b^{\alpha}\chi\mu^{\alpha}\sqrt{\rho_{tot}^{s} + L\sum_{s'}\rho_{tot}^{s'}} \tag{20}$$

with $b^{\alpha} = 2.48\ 10^{-10}\ m$ as the Burgers vector per slip mode, $\chi = 0.9$ as the dislocation interaction parameter, ρ_{tot}^{s} as the total forest density of dislocations, and L as the latent hardening parameter set to 1.0 (Knezevic et al., 2013c; Zecevic and Knezevic, 2018a). The latter term relies on the extended Taylor-type relation (Madec et al., 2003)

$$\tau_{deb}^{\alpha} = 0.086\mu^{\alpha}b^{\alpha}\sqrt{\rho_{deb}}log\left(\frac{1}{b^{\alpha}\sqrt{\rho_{deb}}}\right) \tag{21}$$

where ρ_{deb} is the debris density of dislocations.

The evolution of dislocation densities is such that the deformation-history-dependent directionality is accounted for. To this end, a fraction of accumulated dislocations are considered as reversible to better describe the fluctuations of the hardening rate in non-proportional loadings as introduced in (Rauch et al., 2007). The total dislocation density per slip system consists of the dipole of dislocation densities (forward and reversible dislocations) as

$$\rho_{tot}^{s} = \rho_{for}^{s} + \rho_{rev}^{s^{+}} + \rho_{rev}^{s^{-}} \tag{22}$$

with ρ_{for}^{s} as the forward dislocation density shared by both directions s^{+} and s^{-} and $\rho_{rev}^{s^{+}}$ and $\rho_{rev}^{s^{-}}$ as the reversible dislocation densities on s^{+} and s^{-}, respectively. The evolution of forward dislocations follows the Kocks-Mecking law (Kocks and Mecking, 1981)

$$\frac{\partial\rho_{for}^{s}}{\partial\gamma^{s}} = (1-p)k_{1}^{\alpha}\sqrt{\rho_{for}^{s}+\rho_{rev}^{s}} - k_{2}^{\alpha}(\dot{\varepsilon},T)\rho_{for}^{s} \tag{23}$$

with k_{1}^{α} as a fitting coefficient controlling the rate of dislocation generation, while k_{2}^{α} is a rate-sensitive coefficient controlling the rate of dynamic recovery (Beyerlein and Tomé, 2008), and p is a reversibility constant from 0 to 1 but taken as unity. Given that the parameter divides the increment in the total storage ($k_{1}^{\alpha}\sqrt{\rho_{for}^{s}+\rho_{rev}^{s}}\,d\gamma^{s}$) in a forward ($(1-p)k_{1}^{\alpha}\sqrt{\rho_{for}^{s}+\rho_{rev}^{s}}\,d\gamma^{s}$) increment and a reversible ($pk_{1}^{\alpha}\sqrt{\rho_{for}^{s}+\rho_{rev}^{s}}\,d\gamma^{s}$) increment, the value of unity makes the increment solely reversible. The value of unity is justified by the low accumulated strain level in all simulations presented later in the paper (Ghorbanpour et al., 2020; Kitayama et al., 2013; Zecevic and Knezevic, 2015). The reversible dislocation populations are understood as loosely tangled dislocations that can glide in opposite direction upon load reversal. When the content of dislocation substructures is low, the content of reversible dislocations within the total dislocation content is expected to be large, meaning that the reversibility parameter should take values of close to unity. The buildup of dislocation substructures with the continuation of plastic straining will obstruct dislocation motion in the reverse direction as well as the overall population of dislocations that are loosely tangled will decrease. At this point, the reversibility parameter should take valued lower that unity. The dislocation debris significantly obstructing the reversible motion of dislocations was found to develop in the microstructure at a strain of approximately 0.4 (Kitayama et al., 2013). Since the accumulated strain in all simulations performed here is much less than 0.4, it is reasonable to adopt unity for the value of the reversibility parameter (Kitayama et al., 2013; Zecevic and Knezevic, 2015). While ρ_{for}^{s} is independent of the shearing direction, ρ_{rev}^{s} is the density associated with the shearing direction i.e. if $d\gamma^{s^{+}} > 0$ then $\rho_{rev}^{s} = \rho_{rev}^{s^{+}}$, and if $d\gamma^{s^{-}} > 0$ then $\rho_{rev}^{s} = \rho_{rev}^{s^{-}}$ as.

(If $d\gamma^{s^{+}} > 0$)

$$\frac{\partial\rho_{rev}^{s^{+}}}{\partial\gamma^{s}} = pk_{1}^{\alpha}\sqrt{\rho_{for}^{s}+\rho_{rev}^{s}} - k_{2}^{\alpha}(\dot{\varepsilon},T)\rho_{rev}^{s^{+}} \tag{24}$$

$$\frac{\partial\rho_{rev}^{s^{-}}}{\partial\gamma^{s}} = -k_{1}^{\alpha}\sqrt{\rho_{for}^{s}+\rho_{rev}^{s}}\left(\frac{\rho_{rev}^{s^{-}}}{\rho_{0}^{s}}\right)^{m} \tag{25}$$

with m as a coefficient controlling rate of dislocation recombination, set here to 0.5 (Wen et al., 2015) and ρ_{0}^{s} as the density at the shear reversal on the sth slip system (Kitayama et al., 2013). For $d\gamma^{s-} > 0$, the increments in $\rho_{rev}^{s^{-}}$ and $\rho_{rev}^{s^{+}}$ is calculated in an analogues manner to the above equations. The initial conditions are $\rho_{for}^{s}(\gamma^{s}=0) = \rho_{initial}^{s}$,

$\rho_{rev}^{s^+}(\gamma^s = 0) = 0$ and $\rho_{rev}^{s^-}(\gamma^s = 0) = 0$.

The coefficient k_2^α is obtained using

$$\frac{k_2^\alpha}{k_1^\alpha} = \frac{\chi b^\alpha}{g^\alpha}\left(1 - \frac{k_B T}{D^\alpha (b^\alpha)^3} ln\left(\frac{\dot{\varepsilon}}{\dot{\varepsilon}_0}\right)\right), \tag{26}$$

where, k_B, $\dot{\varepsilon}_0$, g^α and D^α are constants: the Boltzmann constant, a reference strain rate set to 10^7 s^{-1}, and two fitting constant of an effective activation enthalpy and a drag stress, respectively. An increment of the debris development with the rate of recovery is

$$d\rho_{deb} = \sum_s q^\alpha b^\alpha \sqrt{\rho_{deb}} k_2^\alpha \rho_{tot}^s |d\gamma^s|, \tag{27}$$

where q^α is a dislocation recovery rate fitting constant that removes a fraction of α-type dislocations that do not annihilate to become debris.

During forward tensile deformation, the dislocations mostly piled up close to obstacles such as phase or grain boundaries (Yaddanapudi et al., 2021). A strong BE can develop in steels in part as a consequence of easy annihilation of these dislocations formed during prior straining upon strain reversal (Gardey et al., 2005; Wilson and Bate, 1986). The effect is inferred from a decrease in hardness and shrinkage in the diffraction peak widths upon strain reversal (Wilson and Bate, 1986). At the strain reversal, generation of dislocations is momentarily retarded because a fraction of loosely-tangled stored dislocations easily glide in the reverse direction (Beyerlein, 2008). The stress relaxation takes place in which the piled-up dislocations rearrange themselves toward their equilibrium position along with the annihilation of mobile dislocations. These observations of an instantaneous decrease in dislocation density at the strain reversal is an important mechanism for the model along with the dislocation density evolution law. Hence, a fraction of total dislocation density is annihilated upon strain reversals. Continuous reloading of the relaxed sample proceeds with the dislocation unpinning mechanisms with decline in annihilation and increase in multiplication of dislocations (Prasad et al., 2020).

3.2. Backstress law

Plastic deformation of DP steels initiates in the ferrite phase, while the martensite regions remain elastic (Gong et al., 2016). GNDs start to accumulate around the martensite regions inducing a strain gradient. These GNDs and any heterogeneous distribution of stored dislocations are sources of localized hardening and backstress fields (Nesterova et al., 2015). The stress field arising from GNDs will cause traction acting around martensite regions varying with the distance from the martensite. While the overall volume average stress equilibrates to zero, locally a non-zero value of backstress field is present in the ferrite and martensite phases entering the volume average stress (Brown and Stobbs, 1971). As dislocation density in the ferrite phase increases with plastic strain, dislocation structures develop (Yaddanapudi et al., 2021). Concurrently, GNDs continue to accumulate at these structures ensuring compatible deformation. Hence, in addition to backstress fields from GNDs around the martensite regions, there are backstress fields present inside ferrite grains influencing the grain-level plastic deformation. The volume average of these backstress fields also vanish over grains (Mughrabi, 2001).

Strain gradient plasticity model, which calculate backstress fields from GND calculations have been developed within the crystal plasticity finite element frameworks (Evers et al., 2004; Ma et al., 2006a, b, 2007). While higher order SC formulations also exist (Lebensohn et al., 2016; Zecevic et al., 2017b, 2018, 2019a, 2020), the gradients in the model considered here exits only between the grain and the HEM. Since GNDs are not calculated in the model, a phenomenological law is adopted here to approximate the slip system backstress development with plastic strain giving rise to the kinematic hardening. Formulation in which the backstress evolves with the plastic strain on individual slip systems are known as self-internal backstress formulations. A number of similar approaches exist in the literature (Bayley et al., 2006; Beyerlein and Tomé, 2007; Choi et al., 2013; Goh et al., 2003; Harder, 1999; Li et al., 2014; Wollmershauser et al., 2012; Xu and Jiang, 2004; Zecevic and Knezevic, 2015). The advantage of the backstress law used in this work is in its accuracy, simplicity and computational efficiency. The strain gradient plasticity models are much more computationally demanding.

As described earlier, a slip system activates after $\mathbf{m}^s \cdot \boldsymbol{\sigma} - \tau_{bs}^s = \tau_c^s$ condition is fulfilled. Clearly, the condition is governed in part by the evolution of backstress. In our formulation, the backstress evolution law is for individual slip systems in ferrite grains, while the backstress on individual slip systems in martensite grains is obtained from the condition that the volume average of backstress always vanishes.

The backstress calculation in ferrite begins by calculating the backstress tensor per slip system following the implementation presented in (Harder, 1999)

$$\boldsymbol{\sigma}_{bs}^{c,s,f} = (\mathbf{b}^{c,s} \otimes \mathbf{n}^{c,s} + \mathbf{n}^{c,s} \otimes \mathbf{b}^{c,s})\tau_{bs,sys}^s = 2\mathbf{m}^{c,s}\tau_{bs,sys}^s \tag{28}$$

with $\boldsymbol{\sigma}_{bs}^{c,s,f}$ as a backstress tensor and $\tau_{bs,sys}^s$ as a backstress on the slip system. Then the grain backstress tensor is a summation over individual slip systems

$$\boldsymbol{\sigma}_{bs}^{c,f} = 2\sum_{s'} \mathbf{m}^{c,s'} \tau_{bs,sys}^{s'} \tag{29}$$

The slip system backstress is a resolved shear stress from the grain level backstress tensor

$$\tau_{bs}^s = \mathbf{m}^{c,s} \cdot \boldsymbol{\sigma}_{bs}^{c,f} = \tau_{bs,sys}^s + 2\sum_{s'} \mathbf{m}^{c,s} \cdot \mathbf{m}^{c,s'} \tau_{bs,sys}^{s'} \tag{30}$$

with the sum going over all active slip systems and $s' \neq s$.

Ferrite grains must deform plastically to give rise to backstress. The evolution law for backstress during plastic shearing in s^+ direction ($d\gamma^{s^+} > 0$) is

$$\tau_{bs,sys}^{s^+} = \tau_{bs}^{sat}(1 - \exp(-\nu\gamma^{s^+}) \tag{31}$$

$$\tau_{bs,sys}^{s^-} = -A\tau_{bs,sys}^{s^+} \tag{32}$$

where $\tau_{bs,sys}^{s^+}$ and $\tau_{bs,sys}^{s^-}$ are individual backstresses in the two contrary directions per slip system. The law involves τ_{bs}^{sat} as a fitting parameter representing a saturation value for backstress, and A and ν as the additional fitting parameters, while γ^{s^+} is the shear strain accumulated on the sth slip system. Upon the load reversal, a system that was active during prior straining, s^+, unloads and activates in the reverse direction, i.e. s^-. Given that now $d\gamma^{s^-} > 0$, the evolution law is

$$\tau_{bs,sys}^{s^-} = -(A+1)\tau_{bs0}^{s^+} \exp\left(-\frac{\gamma^{s^-}}{\gamma_b}\right) + \tau_{bs0}^{s^+},\ \tau_{bs}^{s^+} = -\frac{1}{A}\tau_{bs}^{s^-}\ if\ \tau_{bs}^{s^-} < 0 \tag{33}$$

$$\tau_{bs,sys}^{s^-} = \tau_{bs}^{sat}(1 - \exp(-\nu\gamma^{s^-})),\ \tau_{bs}^{s^+} = -A\tau_{bs}^{s^-}\ if\ \tau_{bs}^{s^-} > 0 \tag{34}$$

with $\tau_{bs0}^{s^+}$ as the value of backstress at the point of the reversal and γ_b is an additional fitting parameter. The backstress tensor varies from grain-to-grain with a net volume average of $\left\langle \dot{\boldsymbol{\sigma}}_{bs}^{c,f} \right\rangle$ (Brown and Stobbs, 1971).

Note that the rate forms of the equations are needed for $\mathbf{m}^{c,s} \cdot \hat{\boldsymbol{\sigma}}^c - \dot{\tau}_{bs}^{c,s} = \dot{\tau}_c^{c,s}$ as well as for the derivative $\frac{\partial \dot{\tau}_{bs,sys}^s}{\partial \dot{\gamma}^s}$ i.e. for the backstress matrix, $h_{bs}^{ss'}$. The rate forms are

$$\dot{\boldsymbol{\sigma}}_{bs}^{c,f} = 2\sum_{s'} \mathbf{m}^{c,s'} \dot{\tau}_{bs,sys}^{s'} \tag{35}$$

$$\dot{\tau}_{bs}^{s} = \dot{\tau}_{bs,sys}^{s} + 2\sum_{s'} \mathbf{m}^{c,s} \cdot \mathbf{m}^{c,s'} \dot{\tau}_{bs,sys}^{s'} \; and \; s' \neq s \tag{36}$$

with $\dot{\tau}_{bs,sys}^{s} = \frac{\partial \tau_{bs,sys}^{s}}{\partial \gamma^{s}} \dot{\gamma}^{s}$.

The backstress rate in martensite regions is defined using the volume average of backstress rate in ferrite phase, $\left\langle \dot{\boldsymbol{\sigma}}_{bs}^{c,f} \right\rangle$. Given that the overall backstress in the sample vanishes, the rate of backstress in martensite is

$$\left\langle \dot{\boldsymbol{\sigma}}_{bs}^{mr} \right\rangle = -\frac{V_f}{V_m} \left\langle \dot{\boldsymbol{\sigma}}_{bs}^{c,f} \right\rangle \tag{37}$$

with V_f and V_m as the fractions of ferrite and martensite phases, respectively. The backstress on slip systems in martensite grains is

$$\dot{\tau}_{bs}^{c,s,m} = \mathbf{m}^{c,s} \cdot \left\langle \dot{\boldsymbol{\sigma}}_{bs}^{mr} \right\rangle \tag{38}$$

In summary, $\tau_{bs}^{s^+}$, acts opposite from the resolved shear stress on s^+, i.e. $\mathbf{m}^{s^+} \cdot \boldsymbol{\sigma} - \tau_{bs}^{s^+} = \tau_c^s$. Evidently $\tau_{bs}^{s^+}$ lowers the activation stress. Concurrently, $\tau_{bs}^{s^-}$ aids the activation stress on the slip system s^-, i.e. $\mathbf{m}^{s^-} \cdot \boldsymbol{\sigma} - \tau_{bs}^{s^-} = \tau_c^s$. These kinematic effects are the micro-plasticity processes primarily influencing the non-linear unloading and BE.

4. Experimental results

This section presents the experimental results including flow stress and texture data.

4.1. Experimental results for strain reversal tests

Fig. 1 shows measured true stress-true strain curves during tension-compression-tension reversals. The first loading is forward tension to a given strain level. The second loading is compression to zero strain (1st reversal). The third loading is tension to fracture (2nd reversal). The materials exhibit the decreasing hardening rate during the forward tension, which is typical for metals in which the plasticity is carried out by crystallographic slip. At the 1st reversal, the materials show an initial linear portion and then a non-linear portion of unloading. Macro-yield points during unloading at approximately 0.001 offset are indicated (σ_U). The pre-strain level in forward loading increases the magnitude of macro-yield stress, while the extent of the linear elastic unloading is

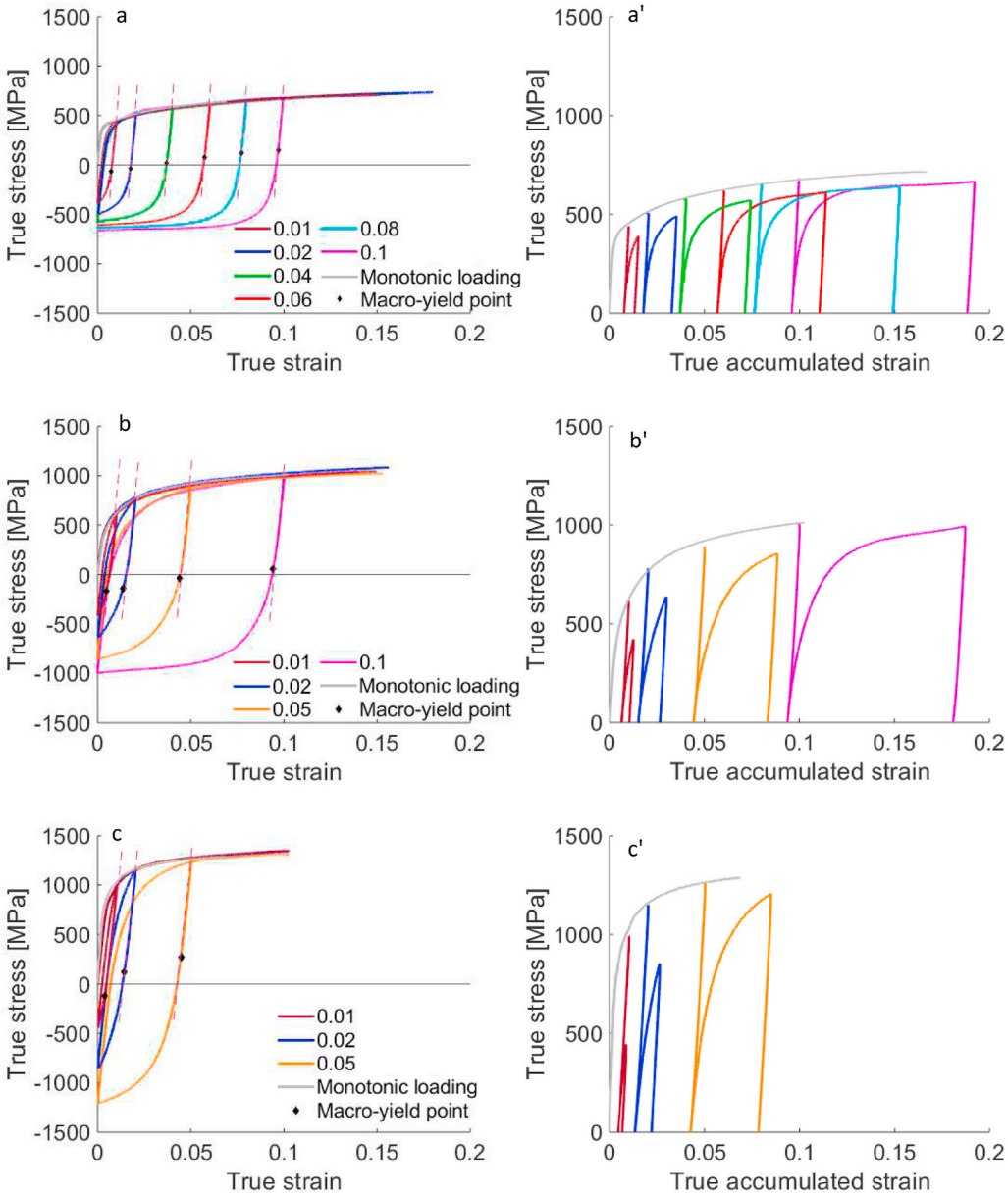

Fig. 1. True stress–true strain curves during strain path reversals at several large strain levels for (a) DP 590, (b) DP 780, and (c) DP 1180 measured along the rolling direction (RD). Macro-yield points during unloading at approximately 0.001 offset are indicated (σ_U). Comparison of forward tension versus the 1st reversal curves as a function of accumulated true strain showing drops in the flow stress i.e. the permanent softening effect upon reversals for (a') DP 590, (b') DP 780, and (c') DP 1180. Legends are shown in the 'unprimend' plots and they apply to the corresponding 'primed' plots.

approximately constant. The extent of the non-linear unloading is enhanced with strength of the steels (Bate and Wilson, 1986; Beyerlein, 2008). The reduction of the yield points between the initial straining and reverse straining is termed as transient softening. The mechanism is equivalent to the BE - the resistance to dislocation motion in the reverse sense is less than in forward straining. Following the transient softening is the permanent softening, which is a lowering of the stress-strain curves when the reverse stress-strain is plotted in the stress direction the same as the prior straining. These phenomena are depicted in the primed figures of Fig. 1. The permanent softening phenomenon was first described in (Hasegawa et al., 1975) during tension-compression loading and also during forward-reverse simple shear loading in (Gracio et al., 2004). The origin of transient and permanent softening is in the backstress and annihilation of dislocations after reversing the glide directions during loading in the reverse direction. Like non-linear unloading, these phenomena are enhanced with strength.

Fig. 2 shows comparisons between the forward tension and the 1st and 2nd reversals to observe the yielding differentials and subsequent hardening rates. As is evident, the transients after the 1st reversal are larger than the transients after the 2nd reversal. As the elasto-plastic transition upon the reversals (1st and the 2nd) is prolonged, the strain hardening rates are reduced compared to those during the forward tension. Although reduced, the strain hardening in compression of DP 590 surpasses that in tension causing positive yield differentials. The positive yield differential increases with pre-strain. The yield differentials for DP 780 and DP 1180 appear negative. The origin of these reloading yield stress differentials is also in the backstress and annihilation of dislocations, as will be described later. Upon macroscopic re-yielding, the rate of strain hardening is restored. The curves after the 2nd reversal evolve towards the forward tension curves.

4.2. Texture characterization

The present work uses the two-phase EPSC constitutive law

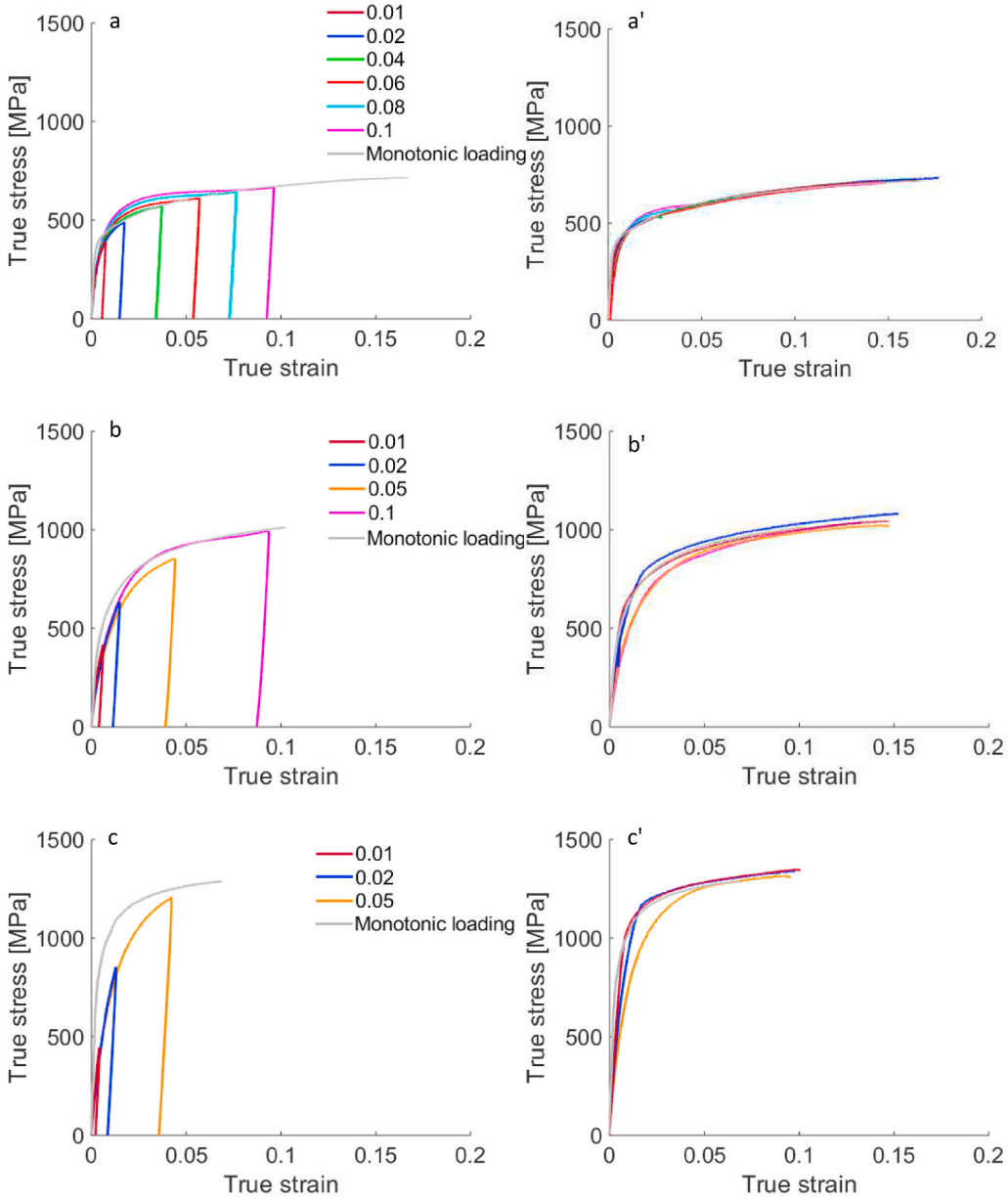

Fig. 2. Comparison of the forward tension versus the 1st reversal (i.e. compression) curves pre-strained in tension to different strain levels for (a) DP 590, DP 780, and (c) DP 1180. Comparison of the forward tension versus the 2nd reversal (i.e. tension) curves pre-strained in tension followed by compression to different strain levels for (a') DP 590, (b') DP 780, and (c') DP 1180. Legends are shown in the 'unprimend' plots and are the same for the corresponding 'primed' plots.

enhanced for a dislocation density law and a backstress law to predict and interpret the above-described phenomena. To initialize the model, in addition to phase fractions, texture is needed. To this end, the measurements of texture were carried out on initial samples of every steel using the High Pressure Preferred Orientation (HIPPO) beam at the pulsed neutron spallation source at Los Alamos National Laboratory, LANSCE. It is a time-of-flight neutron diffractometer for bulk texture characterization of metals at ambient and non-ambient (pressure, temperature, and load) conditions (Wenk et al., 2003). Unlike EBSD, texture measured using neutron diffraction is averaged over mm^3 to cm^3 volumes owing to the deep penetration of thermal neutrons into the metals, combined with a large beam spot sizes of ~0.1–1 cm^2. The count time for the present measurements was approximately 20 min at a proton current of 100 microA. Many inverse pole figures (i.e. in 135 sample directions) are measured to ensure a sufficient coverage for fiting an orientation distribution function (ODF) in a concurrent Rietveld refinement of 135 patterns, including also parameters such as lattice parameters (Wenk et al., 2010). Note that both martensite and ferrite are contained in the measurements as their diffraction peaks overlap. The ODF analyses of the data were done using MAUD (Wenk et al., 2010) with 7.5° resolution and the pole figures are plotted in MTEX (Bachmann et al., 2010). Fig. 3 shows measured pole figures visualizing the initial texture in the steels. Texture in the steels is a typically reported orthotropic rolled texture for body-centered cubic (BCC) metals, where the crystal orientations are concentrated around the γ-fiber and the α-fiber (Bhattacharyya et al., 2015; Holscher et al., 1994; Kocks et al., 1998). The texture intensity reduces with the fraction of martensite.

5. Model calibration and validation

This section begins by calibrating the model using the cyclic tension-compression-tension response of DP 590, DP 780, and DP 1180 steels. The axial deformation processes are simulated by applying strain increments along the rolling direction (RD), while enforcing the normal

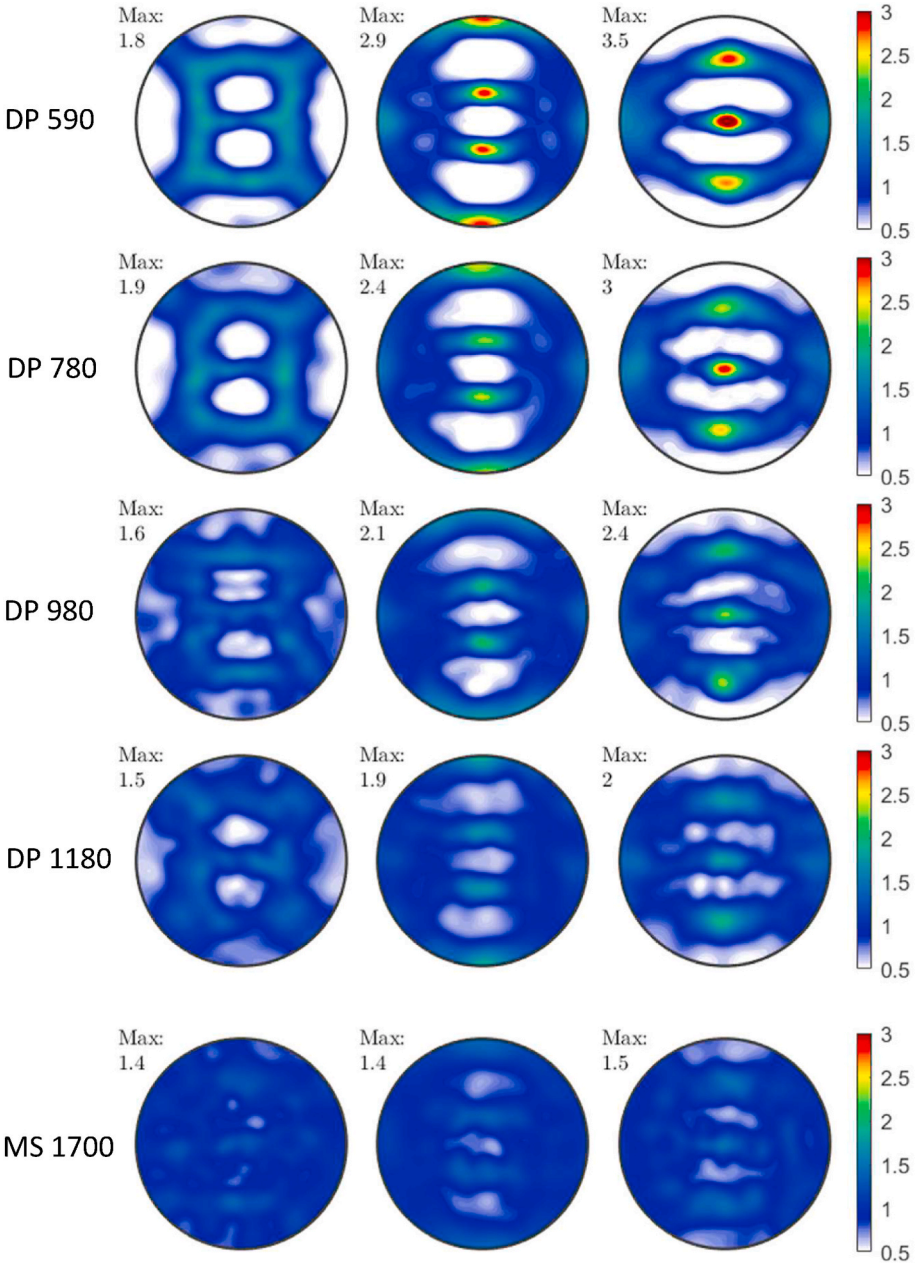

Fig. 3. Stereographic pole figures showing the initial texture in sheets of DP 590 (top), DP 780, DP 980, and DP 1180, and MS 1700 (bottom).

stresses in transverse direction (TD) and normal direction (ND) as well as the shear strains to zero. In the simulations, the measured textures were compacted to 150 weighted orientations for ferrite, while 100 random orientations were used for texture of martensite. Given that DP 590 has ~93% of ferrite, the measured texture for DP 590 can be considered as that of ferrite. Likewise, given that MS 1700 has ~85% of martensite, the measured texture for MS 1700 can be considered as that of martensite. The martensite texture is predominantly random. These two textures are appropriately weighted for the input into the model of every steel. The texture compaction methodology used to represent textures was described in (Barrett et al., 2019; Eghtesad et al., 2018b; Jahedi et al., 2017a; Knezevic and Landry, 2015).

The parameters pertaining to the hardening law for the evolution of slip resistances in ferrite and martensite and the backstress law for ferrite were adjusted using one cyclic tension-compression-tension curve per steel, as each parameter affects a different portion of the curve. The curve deformed to a tensile pre-strain of 0.06 was used for DP 590, while the curves deformed to a tensile pre-strain of 0.05 were used for DP 780 and DP 1180. The identified parameters were fine-tuned (<3% adjustments) by comparing another cyclic curve per steel. The remaining tension-compression-tension curves can be regarded as predictions showing the extrapolation capability of the physically-based EPSC model, which is the main advantage with respect to phenomenological models. The parameters identified per phase are the initial resistance to slip, τ_0^α, trapping rate coefficient, k_1^α, drag stress, D^α and activation barrier for de-pinning, g^α, (Savage et al., 2021a). The identification procedure begins by varying τ_0^α to reproduce initial yielding. Next, k_1^α, is varied such that the initial hardening slope is captured. Next, g^α and D^α are varied to match the hardening rates. Finally, q^α is fit to capture the later stage of the hardening rates. Simultaneously with the hardening parameters, the backstress law parameters for ferrite were calibrated for DP 590, DP 780, and DP 1180. These include the saturation value for backstress τ_{bs}^{sat}, asymmetry factor, A, and coefficients ν and γ_b. Here, both τ_{bs}^{sat} and A are varied simultaneously to obtain the unloading and asymmetric yield at load reversals. Once these are achieved, tuning ν and γ_b simply provides better fits. Next, the monotonic curves were simulated. While these for DP 590, DP 780, and DP 1180 are predictions, some parameters were slightly adjusted to fit the data for DP 980 and MS 1700. The established parameters are given in Table 3. Note that the hardening parameters per phase are the same for every steel, except D^α and the initial content of dislocation density per phase.

The initial slip resistances, τ_0^α, were first estimated 75.4, 77.8, 80.8, 93.9, 95.9 [MPa] for ferrite and 501.8, 503.5, 550.4, 652.2, 774.2 [MPa] for martensite per steel, DP 590, DP 780, DP 980, DP 1180, and MS 1700, respectively. These values include the contribution of the initial dislocation density content. Given the measured values of dislocation density per phase for DP 1180 provided in (Yaddanapudi et al., 2021), we estimated the friction term of slip resistance, τ_{00}^α by subtracting the contribution of the initial dislocation density from τ_0^α for DP 1180. Keeping the same friction stress for every steel, we estimated the initial dislocation density per phase for every steel, $\sum_s \rho_{initial}^s$. Dislocation density increases with the content of martensite per steel. The expansion in volume during austenite to martensite phase transformation causes the deformation of ferrite phase and accumulation dislocations around martensite regions (Calcagnotto et al., 2010; Kadkhodapour et al., 2011). Therefore, the content of initial dislocation density is larger in steels containing more martensite. The higher the content, the higher the strength. It should also be noted that, in addition to the content of dislocations, chemical composition (i.e. the carbon content) influence the slip resistance and drag stress of the steels. This is true especially for martensite (Das et al., 2017). Therefore, the estimate for τ_{00}^α is an approximation.

Fig. 4 shows the comparison between measured and simulated tension-compression-tension curves for the three steels. The multiple-range hysteresis curves are modeled with reasonable accuracy. In particular, the model is capable of reproducing the features specific to the load reversal behavior of the steels including the hardening rates during forward loading, non-linear unloading, BE, permanent softening and subsequent hardening rates. Fig. 5 shows the predictions for the monotonic data. The basic properties of the steels are listed in Table 4. The model is further experimentally validated by predicting a set of data recorded under variable strain ranges and mean strains for DP 780 and DP 1180. The model is able to capture these complex data sets also with good accuracy as shown in Fig. 6. Although the model captures the yield point in the first cycle, re-yielding in the subsequent cycles is often over-predicted. Model modifications such as including spreads of field variables over ellipsoids could improve these predictions. Such spreads have been incorporated in a visco-plastic SC formulation (Zecevic et al., 2017b).

6. Discussion

This work presents comprehensive monotonic and load reversal data for five dual phase (DP) steels and is concerned with interpreting the data using a crystal plasticity model, which considers microstructural evolution and the directionality of single-crystal level deformation mechanisms. The model is the EPSC formulation (Zecevic et al., 2016b), which incorporates a dislocation density-based hardening law (Beyerlein and Tomé, 2008) advanced to account for dissolution of dislocations upon load reversal and a slip system-level backstress law.

The load reversal data recorded for DP steels showed the typical

Table 3

a. Fitting parameters pertaining to the evolution of slip resistance for $\{110\}\langle 1\bar{1}1\rangle$ and $\{112\}\langle 11\bar{1}\rangle$ slip modes in ferrite (F) and martensite (M) common for all steels. The Burgers vector is 2.48e-10 m. Table 3b. Fitting parameters pertaining to the evolution of slip resistance for $\{110\}\langle 1\bar{1}1\rangle$ and $\{112\}\langle 11\bar{1}\rangle$ slip modes in ferrite (F) and martensite (M) per steel. Table 3c. Fitting parameters pertaining to the evolution of backstress in ferrite per steel.

Parameter					F					M
$k_1^\alpha[m^{-1}]$					2.5e8					1.5e8
τ_{00}^α [MPa]					75					500
g^α					0.009					0.01
q^α					20					20
Parameter	DP 590 (F)	DP 590 (M)	DP 780 (F)	DP 780 (M)	DP 980 (F)	DP 980 (M)	DP 1180 (F)	DP 1180 (M)	MS 1700 (F)	MS 1700 (M)
$\sum_s \rho_{initial}^s[m^{-2}]$	3.4e9	4.08e10	3.4e10	5.08e10	4.37e10	1.46e11	3.14e12	1.47e13	4e12	4.92e14
D^α [MPa]	650	700	700	750	700	780	800	850	850	900

Parameters	DP 590 (F)	DP 780 (F)	DP 1180 (F)
$\tau_{bs}^{sat}[MPa]$	35	110	195
ν	1000	1000	1000
γ_b	0.001	0.003	0.005
A	2	2	2

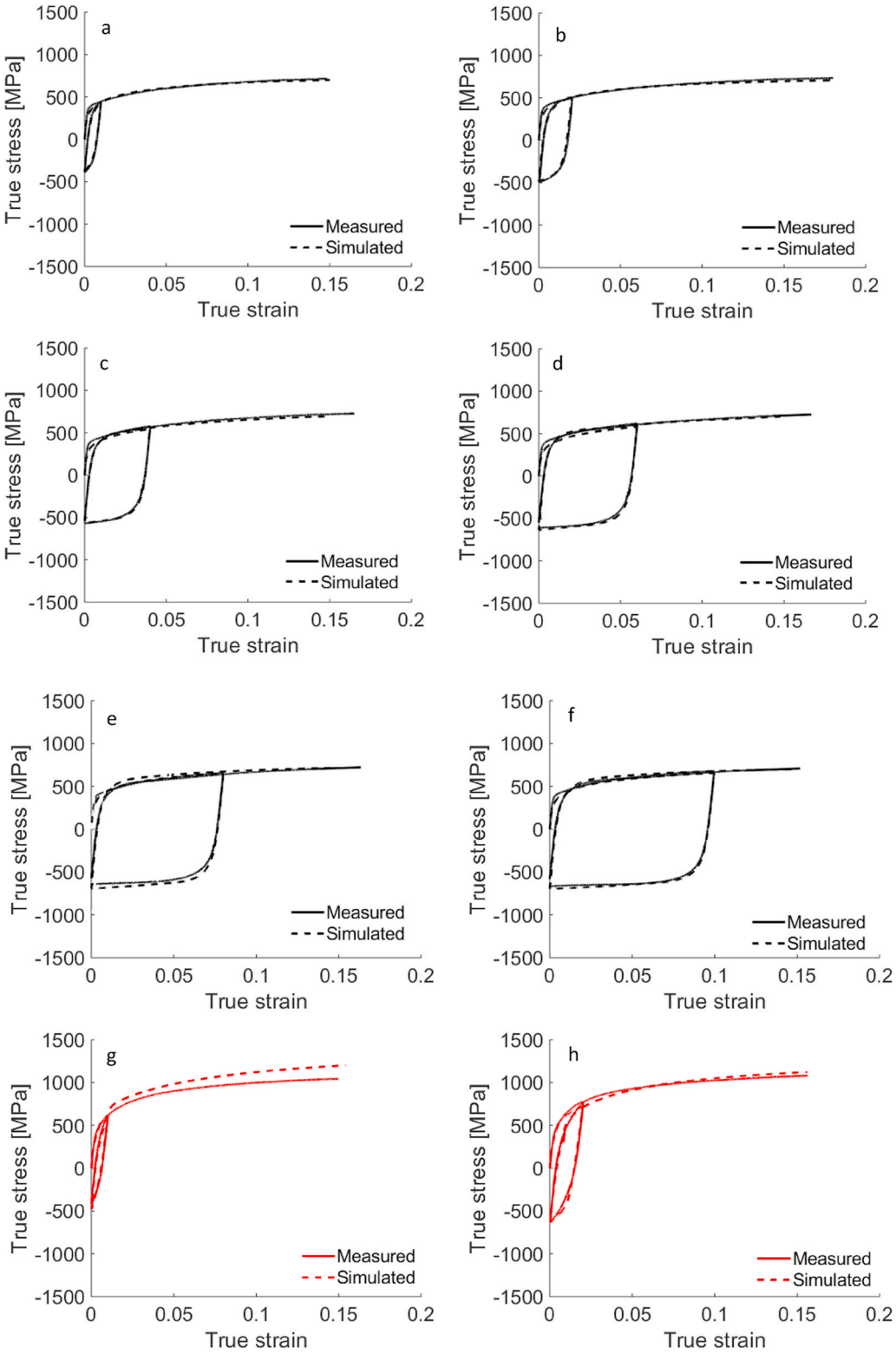

Fig. 4. Comparison of measured and simulated true stress-true strain response during strain path load reversals for (a–f) DP 590, (g–j) DP 780, and (k–m) DP 1180.

decreasing hardening rate during forward tension, a linear and then a non-linear unloading, followed by the BE, and a slight shift in the hardening rate during continuous straining. The data were used to calibrate and critically validate the EPSC model. The good performance of the model in capturing such elasto-plastic deformation characteristics is a consequence of accounting for kinematic hardening at the slip system-level through the evolution law for backstress for both ferrite and martensite and dislocation annihilation physical mechanism to reflect the experimentally observed decrease in dislocation density upon strain reversal. Additionally, the model is correctly initialized with the experimentally measured texture, phase fractions, and dislocation density per phase. From the comparisons between data and predictions, the

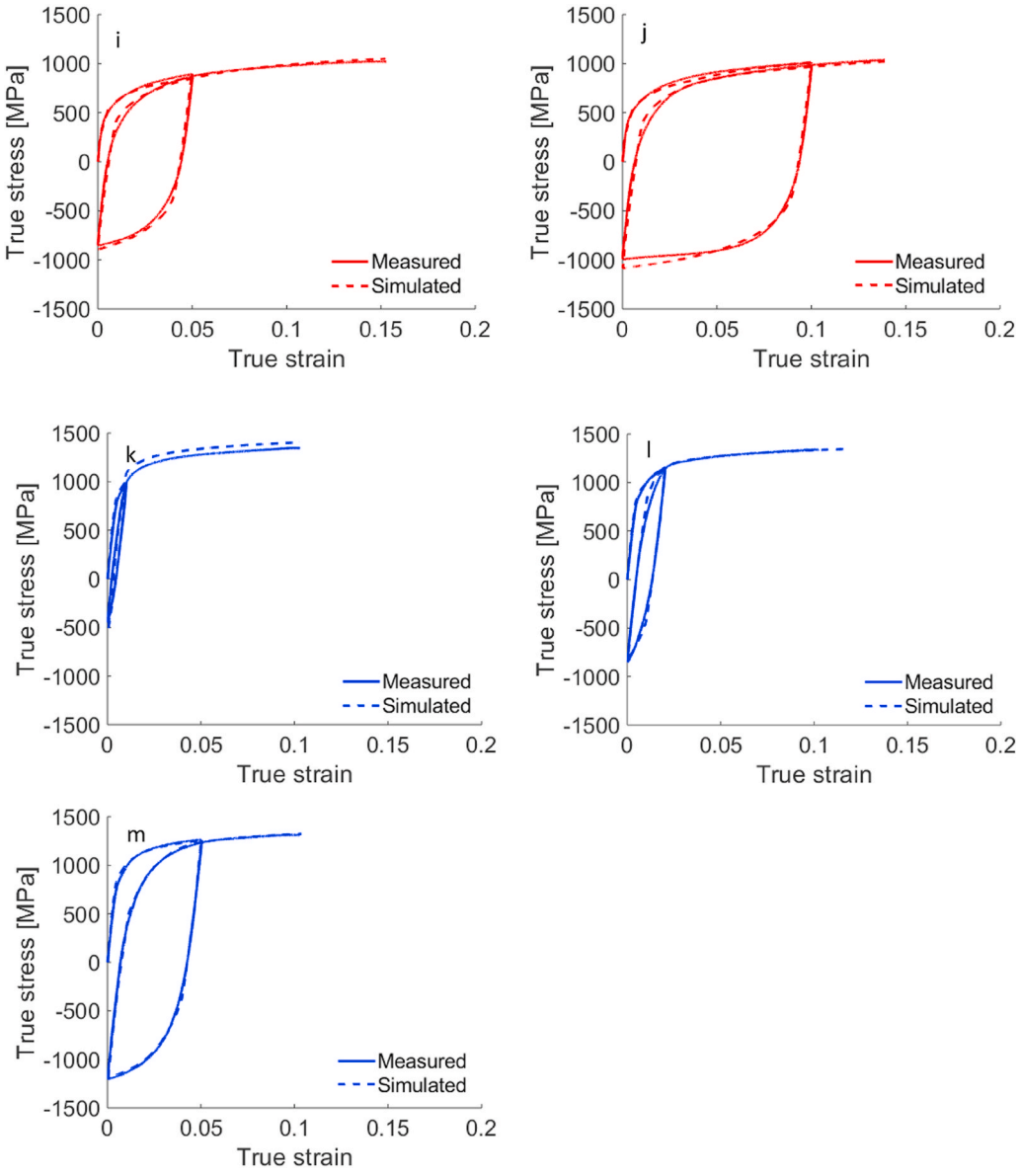

Fig. 4. (*continued*).

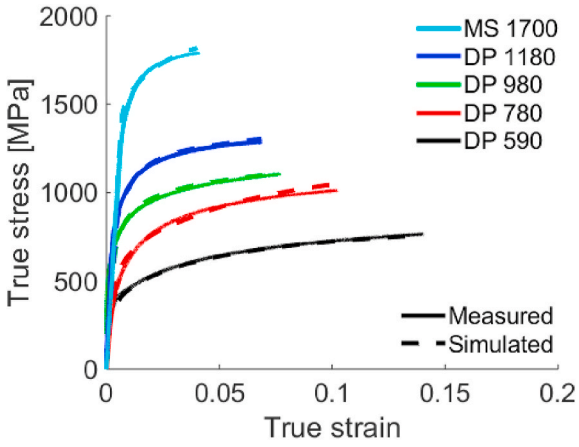

Fig. 5. Comparison of measured and predicted true stress-true strain response in simple tension for the studied steels.

Table 4
Properties based on the engineering curves for the steel sheets.

	DP 590 (RD)	DP 780 (RD)	DP 980 (RD)	DP 1180 (RD)	MS 1700 (RD)
0.2% offset yield stress (MPa)	407	504	630	840	1487
UTS (MPa)	663	913	1090	1288	1778
Eng. strain at UTS	0.146	0.108	0.086	0.072	0.041
Eng. strain at fracture	0.187	0.139	0.111	0.077	0.042

aim is to provide insights into various aspects of the material response during load reversals.

It is observed that the tensile hysteresis loops do not overlap with the monotonic tensile curves. Several additional parameters can be defined from the differences to further discuss the load reversal deformation characteristics of the steels. Fig. 7a illustrates these parameters using representative enlarged areas of the stress-strain curves. The parameters are the reloading stress differential, $\Delta\sigma_h$, reloading softening stress, $\Delta\sigma_s$, and ratcheting strain, ε_Δ. These specific parameters are quantified for DP

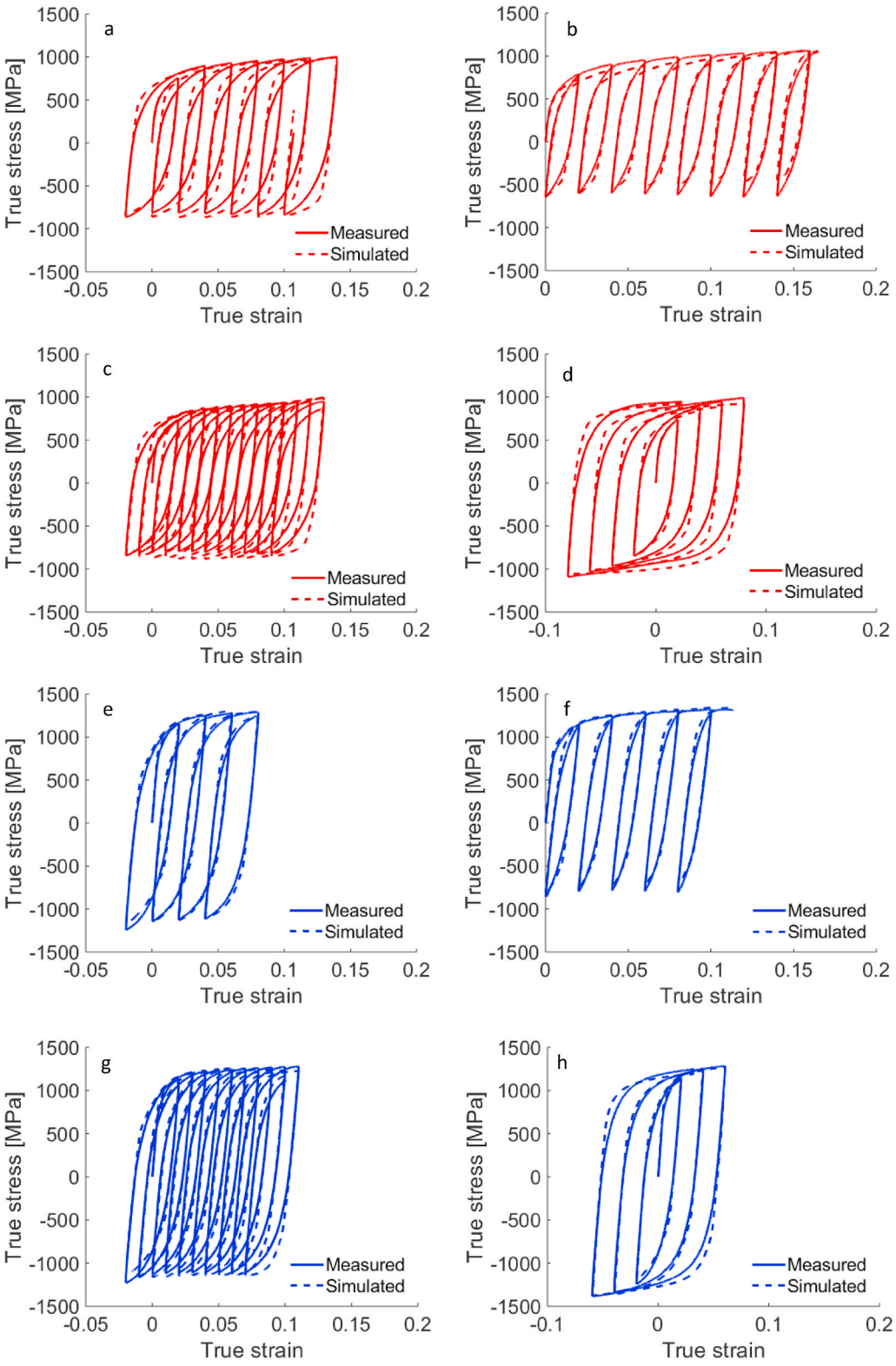

Fig. 6. Comparison of measured and predicted true stress-true strain response during large strain reversals for (a–d) DP 780, and (e–h) DP 1180. The strain path in (a, e) is: 0 → 0.02 → −0.02 → 0.04 → 0 → 0.06 … up to fracture with the strain amplitude of 0.04 and the mean strain increase of 0.02 per cycle. The strain path in (b, f) is: 0 → 0.02 → 0 → 0.04 → 0.02 → 0.06 … up to fracture with the strain amplitude of 0.02 and the mean strain increase of 0.02 per cycle. The strain path in (c, g) is: 0 → 0.02 → −0.02 → 0.03 → −0.01 → 0.04 … up to fracture with the strain amplitude of 0.04 and the mean strain increase of 0.01 per cycle. The strain path in (d, h) is: 0 → 0.02 → −0.02 → 0.04 → −0.04 → 0.06 … up to fracture.

780 and DP 1180. Additionally, the unloading deviation stress $\Delta\sigma$ is quantified for DP 590, DP 780, and DP 1180. The values of these individual parameters are discussed as a function of martensite and loading.

The reloading yield stress differential under tension (the differential between initial tension and 2nd reversal), $\Delta\sigma_h$, as a function of the applied tensile pre-strain is shown in Fig. 7b. The differential increases with plastic strain and content of dislocations. While positive for DP 590, it is negative for DP 780 and DP 1180. Evidently, the increasing content of martensite weakens the reloading yield effect, which is attributed to the increase in backstress in the microstructure with martensite. The evolution of reloading softening stress with the tensile pre-strain for the investigated steels is shown in Fig. 7c based on the data for two strain amplitudes, 0.02 and 0.04. Since the results are similar for both strain amplitudes, likely no appreciable plasticity occurred in compression for

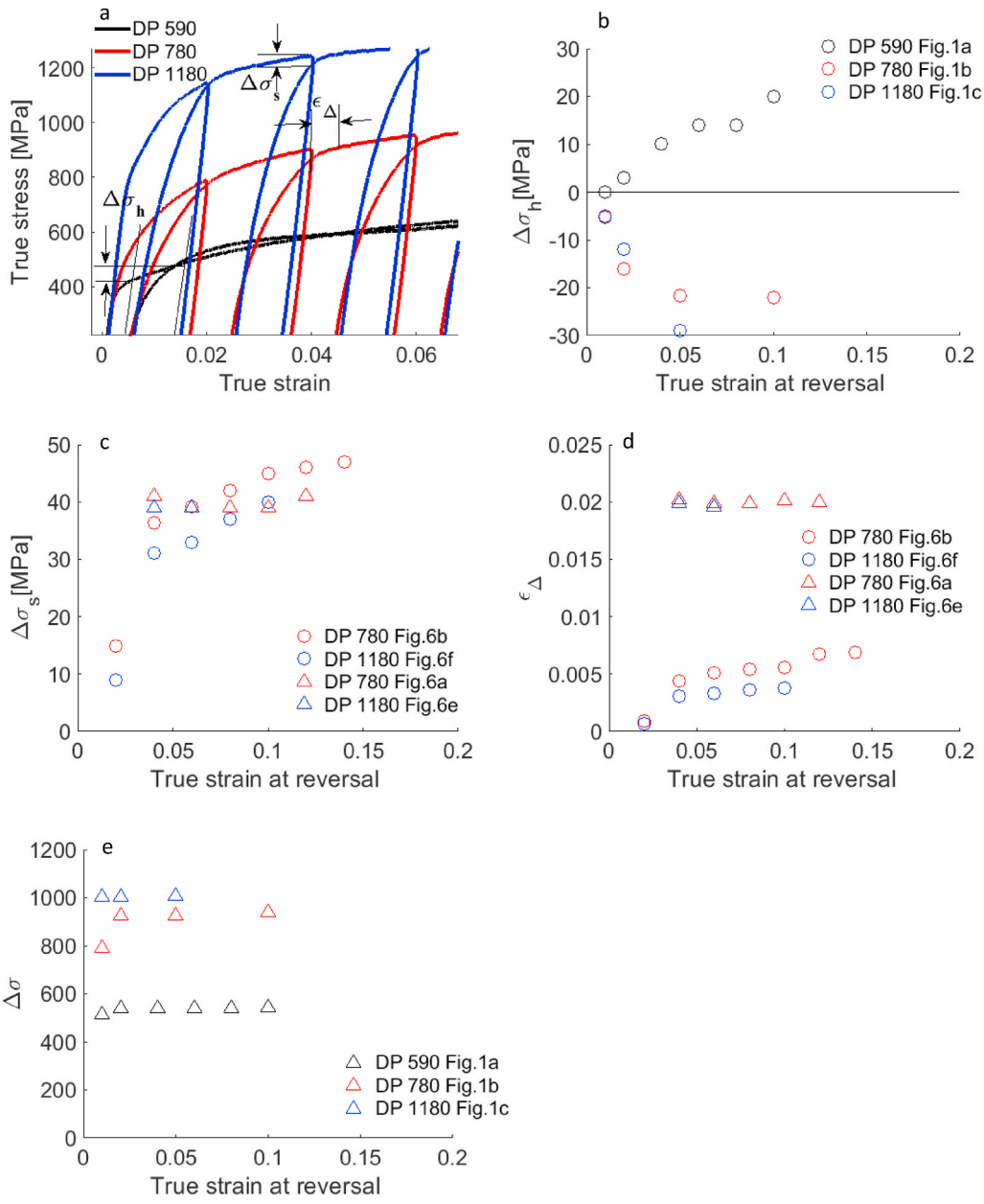

Fig. 7. (a) An illustration to define the reloading yield stress differential under tension ($\Delta\sigma_h$), reloading softening stress ($\Delta\sigma_s$), and ratcheting strain (ε_Δ) parameters. (b) Comparison of $\Delta\sigma_h$ versus true strain levels for 1st reversal. (c) Comparison of $\Delta\sigma_s$ versus true strain levels for tension. (d) Comparison of ε_Δ versus true strain levels for tension. (e) Unloading deviation stress ($\Delta\sigma = \sigma_L - \sigma_U$), where σ_L is the true stress at the end of a pre-load and σ_U is the macro-yield during unload at approximately 0.001 offset.

both datasets. The softening effects is slightly larger for the softer steel. Fig. 7d shows the ratcheting strain evolution with the tensile pre-strain. Overall, the ratcheting strain shows a similar evolution trend as the reloading softening effect because the ratcheting strain results from the softening effect but, in contrast, increases with the strain amplitude and underlying loading nonlinearity. The less strong/stiff DP 780 has the ratcheting strain a bit greater than the more strong/stiff DP 1180. The unloading deviation stress, $\Delta\sigma$, is shown in Fig. 7e as a function of the applied pre-strain in tension. The deviation increases with the strength of the steels.

The model reveals that the backstress predominately controls the non-linear unloading deformation and the BE along with the reloading yield effect, while the evolution of dislocation density plays a role in capturing the BE and, more importantly, in predicting the hardening rates. Fig. 8 shows the evolution of backstress with the accumulated shear strain in a randomly selected grain per phase for a slip system with the highest activity in the selected grain. It should be noted that stress in each grain is a consequence of the applied stress, intergranular interaction stress, and backstress. The backstress in ferrite hinders the process of plastic deformation, since it acts against the applied field. In contrast, the backstress in the martensite phase is opposite to the backstress present in the ferrite acting with the applied field because the volume average backstress in the material vanishes. Note the line type in Fig. 8. The backstress in ferrite will aids the activation upon the reversal. The tradeoff between the magnitude of backstress per phase (Fig. 8) over the steels is a consequence of the volume fraction of ferrite versus martensite per steel (Table 2). Specifically, the increasing content of martensite weakens the reloading yield effect because it increases the backstress in the microstructure (Fig. 8). Note that the magnitude of backstress in martensite is driven by the magnitude of backstress in ferrite but scales inversely with the volume fraction of martensite. The tradeoff governs the unloading and subsequent yield differential per steel. The fact that martensite is deforming elastically longer than ferrite is also contributing to the tradeoff, especially after the reversal.

The annihilation of dislocation density is another important mechanism for accurate predictions of stress levels during cyclic deformation since the hardening rates upon load reversals are controlled primarily by the strain-path sensitive evolution of dislocation density. Fig. 9 shows

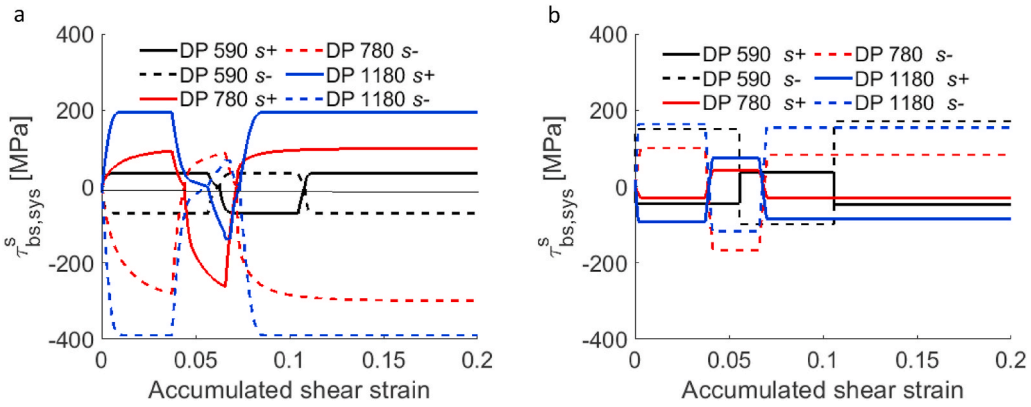

Fig. 8. Evolution of backstress with accumulated shear strain in a randomly selected (a) ferrite grain and (b) a randomly selected martensite grain for an sth slip system with the highest activity per grain during forward tension followed by the 1st and the 2nd reversal for DP 590 (Fig. 4d), DP 780 (Fig. 4i), and DP 1180 (Fig. 4m). The same crystal orientation and the same slip system per phase are selected for every material.

the volume average dislocation density evolution during the cyclic deformation of DP 1180. Such plots for other steels look similar and are not provided. The plot shows that the dislocation density evolves much more rapidly in ferrite than in martensite. The dissolution of the dislocations upon load reversal is essential in predicting the changes in the hardening rates. Evidently some deformation can be accommodated without a large increase in dislocation density. These results agree with the constitutive assumptions invoked in developing cyclic plasticity models (Ohno, 1982; Ohno and Kachi, 1986).

7. Conclusions

The monotonic response of DP 590, DP 780, DP 980, DP 1180, and MS 1700 and the large strain cyclic response of DP 590, DP 780, and DP 1180 steel sheets were measured. The large body of cyclic data showed consistently the typical decreasing hardening rate during forward tension, a linear and then a non-linear unloading, followed by the BE, and some shift in the hardening rate during continuous straining. Since the cyclic loops did not overlap with the monotonic curves, parameters such as the reloading yield stress differential, reloading softening stress, ratcheting strain, and unloading deviation stress were identified and quantified. The pre-strain level in forward loading increased the magnitude of macro-yield stress, while the unloading deviation stress was approximately constant. The extent of the non-linear unloading increased with strength of the steels. Since the elasto-plastic transition upon the reversals (1st and the 2nd) was prolonged, the strain hardening

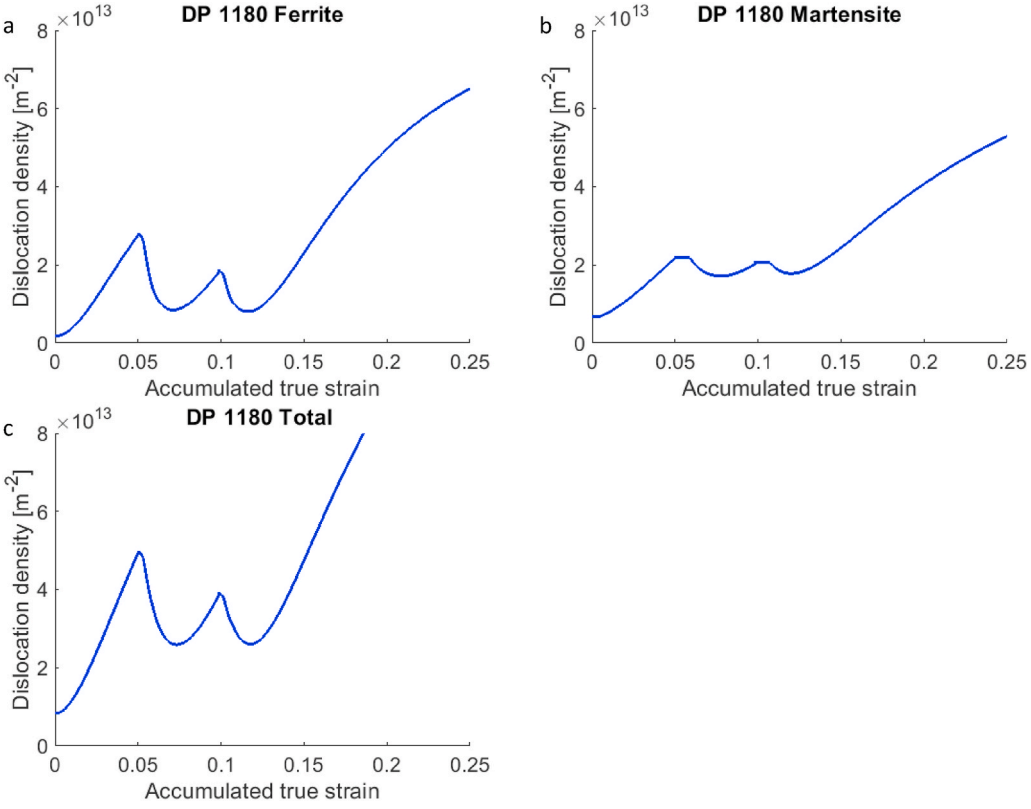

Fig. 9. Evolution of total dislocation density ($\sum_s \rho^s_{tot}$) in (a) ferrite, (b) martensite, and (c) combined ferrite + martensite during load reversal deformation of DP 1180 (Fig. 4m).

rates reduced compared to those during the forward tension. Although reduced, the strain hardening in compression of DP 590 surpassed that in tension and also induced positive yield differentials under tension. The positive yield differential increased with pre-strain. In contrast, the yield differentials for DP 780 and DP 1180 were negative. The reloading softening stress and ratcheting strain scaled inversely with the strength of the steels. Upon yielding after the load reversal, the rates of strain hardening were quickly restored. Like non-linear unloading, the permanent softening was enhanced with strength.

The data were used to calibrate and critically validate an EPSC model developed for two-phase steels. The model features sub-models including a dislocation density-based hardening law and a slip system-level kinematic back-stress law for load reversals. It was shown that the model successfully reproduces the flow response of the steels during monotonic and cyclic deformation to various levels of plastic pre-strains. Specifically, hardening rates, non-linear unloading, and the BE were captured. Significantly, the model achieved excellent agreement for all data using a single set of parameters per phase except for one parameter, which varied from steel to steel. Such good performances of the model in capturing the deformation characteristics were a consequence of accounting for kinematic hardening at the slip system-level through the evolution law for backstress for both ferrite and martensite and dislocation annihilation physical mechanism to reflect the experimentally observed decrease in dislocation density upon strain reversals. Additionally, the model was correctly initialized with the experimentally measured texture, phase fractions, and dislocation density per phase. The combination of comprehensive experimental data and modeling results allowed us to infer that the tradeoff between the magnitude of backstress per phase and the volume fraction of ferrite versus martensite per steel determined the unloading and subsequent yield differential per steel, while the dissolution of dislocations facilitated capturing the hardening rates during load reversal deformation. Specifically, the increasing content of martensite weakened the reloading yield effect because it increased the overall backstress in the microstructure. As the phenomena captured by the standalone model have major implications on the accuracy of simulations of metal forming processes of steels, the model will be used in the FEM forming simulations treating complex, non-monotonic deformation conditions in the future works.

Credit author statement

Sowmya Daroju; Software, Validation, Formal analysis, Investigation, Visualization, Toshihiko Kuwabara; Methodology, Investigation, Writing – review & editing, Marko Knezevic; Conceptualization, Methodology, Resources, Writing – original draft, Writing – review & editing, Supervision, Project administration, Funding acquisition

Declaration of competing interest

The authors declare that they have no known competing financial interests or personal relationships that could have appeared to influence the work reported in this paper.

Acknowledgments

This research was sponsored by the U.S. National Science Foundation and accomplished under the CAREER grant no. CMMI-1650641.

References

Abel, A., 1987. Historical Perspectives and Some of the Main Features of the Bauschinger Effect, Materials Forum. Institute of Metals and Materials Australasia, pp. 11–26.
Ardeljan, M., Beyerlein, I.J., McWilliams, B.A., Knezevic, M., 2016a. Strain rate and temperature sensitive multi-level crystal plasticity model for large plastic deformation behavior: application to AZ31 magnesium alloy. Int. J. Plast. 83, 90–109.
Ardeljan, M., Knezevic, M., 2018. Explicit modeling of double twinning in AZ31 using crystal plasticity finite elements for predicting the mechanical fields for twin variant selection and fracture analyses. Acta Mater. 157, 339–354.
Ardeljan, M., McCabe, R.J., Beyerlein, I.J., Knezevic, M., 2015. Explicit incorporation of deformation twins into crystal plasticity finite element models. Comput. Methods Appl. Mech. Eng. 295, 396–413.
Ardeljan, M., Savage, D.J., Kumar, A., Beyerlein, I.J., Knezevic, M., 2016b. The plasticity of highly oriented nano-layered Zr/Nb composites. Acta Mater. 115, 189–203.
Armstrong, P.J., Frederick, C.O., 1966. A Mathematical Representation of Multiaxial Bauschinger Effect. Berkeley nuclear laboratories.
Bachmann, F., Hielscher, R., Schaeben, H., 2010. Texture analysis with MTEX–free and open source software toolbox. Solid State Phenom. 160, 63–68.
Barrett, T.J., Eghtesad, A., McCabe, R.J., Clausen, B., Brown, D.W., Vogel, S.C., Knezevic, M., 2019. A generalized spherical harmonics-based procedure for the interpolation of partial datasets of orientation distributions to enable crystal mechanics-based simulations. Materialia 6, 100328.
Barrett, T.J., Knezevic, M., 2019. Deep drawing simulations using the finite element method embedding a multi-level crystal plasticity constitutive law: experimental verification and sensitivity analysis. Comput. Methods Appl. Mech. Eng. 354, 245–270.
Barrett, T.J., Knezevic, M., 2020. Modeling material behavior during continuous bending under tension for inferring the post-necking strain hardening response of ductile sheet metals: application to DP 780 steel. Int. J. Mech. Sci. 174, 105508.
Barrett, T.J., McCabe, R.J., Brown, D.W., Clausen, B., Vogel, S.C., Knezevic, M., 2020. Predicting deformation behavior of α-uranium during tension, compression, load reversal, rolling, and sheet forming using elasto-plastic, multi-level crystal plasticity coupled with finite elements. J. Mech. Phys. Solid. 138, 103924.
Barrett, T.J., Savage, D.J., Ardeljan, M., Knezevic, M., 2018. An automated procedure for geometry creation and finite element mesh generation: application to explicit grain structure models and machining distortion. Comput. Mater. Sci. 141, 269–281.
Bate, P.S., Wilson, D.V., 1986. Analysis of the bauschinger effect. Acta Metall. 34, 1097–1105.
Bauschinger, J., 1886. Über die Veränderung der Elasticitätsgrenze und Festigkeit des Eisen und Stahls durch Strecken und Quetschen, durch Erwarmen und Abkühlen und durch oftmal wiederholte Beanspruchung. In: Mitteilungen aus dem mechanisch-technischen Laboratorium der k. polytechnischen Schule, 1877-1836.
Bayley, C.J., Brekelmans, W.A.M., Geers, M.G.D., 2006. A comparison of dislocation induced back stress formulations in strain gradient crystal plasticity. Int. J. Solid Struct. 43, 7268–7286.
Beyerlein, I.J., 2008. Plastic behavior of metals in reverse straining after large pre-strains. Mater. Sci. Forum 579, 41–60.
Beyerlein, I.J., Tomé, C.N., 2007. Modeling transients in the mechanical response of copper due to strain path changes. Int. J. Plast. 23, 640–664.
Beyerlein, I.J., Tomé, C.N., 2008. A dislocation-based constitutive law for pure Zr including temperature effects. Int. J. Plast. 24, 867–895.
Bhadeshia, H.K.D.H., 2002. TRIP-assisted steels? ISIJ Int. 42, 1059–1060.
Bhargava, M., Chakrabarty, S., Barnwal, V.K., Tewari, A., Mishra, S.K., 2018. Effect of microstructure evolution during plastic deformation on the formability of transformation induced plasticity and quenched & partitioned AHSS. Mater. Des. 152, 65–77.
Bhattacharyya, A., Knezevic, M., Abouaf, M., 2015. Characterization of crystallographic texture and intra-grain morphology in cross-rolled tantalum. Metall. Mater. Trans. 46, 1085–1096.
Brown, L.M., Stobbs, W.M., 1971. The work-hardening of copper-silica: I. A model based on internal stresses, with No plastic relaxation. Phil. Mag. 23, 1185–1199.
Calcagnotto, M., Adachi, Y., Ponge, D., Raabe, D., 2011. Deformation and fracture mechanisms in fine- and ultrafine-grained ferrite/martensite dual-phase steels and the effect of aging. Acta Mater. 59, 658–670.
Calcagnotto, M., Ponge, D., Demir, E., Raabe, D., 2010. Orientation gradients and geometrically necessary dislocations in ultrafine grained dual-phase steels studied by 2D and 3D EBSD. Mater. Sci. Eng., A 527, 2738–2746.
Calcagnotto, M., Ponge, D., Raabe, D., 2012. Microstructure control during fabrication of ultrafine grained dual-phase steel: characterization and effect of intercritical annealing parameters. ISIJ Int. 52, 874–883.
Cantara, A.M., Zecevic, M., Eghtesad, A., Poulin, C.M., Knezevic, M., 2019. Predicting elastic anisotropy of dual-phase steels based on crystal mechanics and microstructure. Int. J. Mech. Sci. 151, 639–649.
Chaboche, J., Rousselier, G., 1983. On the plastic and viscoplastic constitutive equations—Part I: rules developed with internal variable concept. J. Pressure Vessel Technol. 105, 153–158.
Chaboche, J.L., 1977. Viscoplastic constitutive equations for the description of cyclic and ansiotropic behavior of metals. In: XVIIth Polish Solid Mechanics Conference. Bulletin de l'Académie Polonaise des Sciences, Série Sciences et Techniques, pp. 33–41.
Chaboche, J.L., 2008. A review of some plasticity and viscoplasticity constitutive theories. Int. J. Plast. 24, 1642–1693.
Choi, S.H., Kim, E.Y., Woo, W., Han, S.H., Kwak, J.H., 2013. The effect of crystallographic orientation on the micromechanical deformation and failure behaviors of DP980 steel during uniaxial tension. Int. J. Plast. 45, 85–102.
Cullen, G.W., Korkolis, Y.P., 2013. Ductility of 304 stainless steel under pulsed uniaxial loading. Int. J. Solid Struct. 50, 1621–1633.
Das, A., Ghosh, M., Tarafder, S., Sivaprasad, S., Chakrabarti, D., 2017. Micromechanisms of deformation in dual phase steels at high strain rates. Mater. Sci. Eng., A 680, 249–258.

Demir, E., Raabe, D., 2010. Mechanical and microstructural single-crystal Bauschinger effects: observation of reversible plasticity in copper during bending. Acta Mater. 58, 6055–6063.
Deng, N., Kuwabara, T., Korkolis, Y.P., 2015. On the Non-linear Unloading Behavior of a Biaxially Loaded Dual-phase Steel Sheet (in preparation).
Dotsenko, V.I., 1979. Stress relaxation in crystals. Phys. Status Solidi 93, 11–43.
Eghtesad, A., Barrett, T.J., Germaschewski, K., Lebensohn, R.A., McCabe, R.J., Knezevic, M., 2018a. OpenMP and MPI implementations of an elasto-viscoplastic fast Fourier transform-based micromechanical solver for fast crystal plasticity modeling. Adv. Eng. Software 126, 46–60.
Eghtesad, A., Barrett, T.J., Knezevic, M., 2018b. Compact reconstruction of orientation distributions using generalized spherical harmonics to advance large-scale crystal plasticity modeling: verification using cubic, hexagonal, and orthorhombic polycrystals. Acta Mater. 155, 418–432.
Eghtesad, A., Knezevic, M., 2020. High-performance full-field crystal plasticity with dislocation-based hardening and slip system back-stress laws: application to modeling deformation of dual-phase steels. J. Mech. Phys. Solid. 134, 103750.
Eghtesad, A., Knezevic, M., 2021a. Modeling cyclic plasticity of additively manufactured alloy Mar-M-509 using a high-performance spectral-based micromechanical model. Appl. Eng. Sci. 7, 100065.
Eghtesad, A., Knezevic, M., 2021b. A full-field crystal plasticity model including the effects of precipitates: Application to monotonic, load reversal, and low-cycle fatigue behavior of Inconel 718A. Mater. Sci. Eng. A 803, 140478.
Eghtesad, A., Zecevic, M., Lebensohn, R.A., McCabe, R.J., Knezevic, M., 2018c. Spectral database constitutive representation within a spectral micromechanical solver for computationally efficient polycrystal plasticity modelling. Comput. Mech. 61, 89–104.
Eshelby, J.D., 1957. The determination of the elastic field of an ellipsoidal inclusion, and related problems. Proc. Roy. Soc. Lond. A 241, 376–396.
Evers, L.P., Brekelmans, W.A.M., Geers, M.G.D., 2004. Non-local crystal plasticity model with intrinsic SSD and GND effects. J. Mech. Phys. Solid. 52, 2379–2401.
Feather, W.G., Ghorbanpour, S., Savage, D.J., Ardeljan, M., Jahedi, M., McWilliams, B.A., Gupta, N., Xiang, C., Vogel, S.C., Knezevic, M., 2019. Mechanical response, twinning, and texture evolution of WE43 magnesium-rare earth alloy as a function of strain rate: experiments and multi-level crystal plasticity modeling. Int. J. Plast. 120, 180–204.
Feather, W.G., Lim, H., Knezevic, M., 2020. A numerical study into element type and mesh resolution for crystal plasticity finite element modeling of explicit grain structures. Comput. Mech.
Feather, W.G., Savage, D.J., Knezevic, M., 2021. A crystal plasticity finite element model embedding strain-rate sensitivities inherent to deformation mechanisms: application to alloy AZ31. Int. J. Plast. 143, 103031.
Feng, Z., Yoon, S.-Y., Choi, J.-H., Barrett, T.J., Zecevic, M., Barlat, F., Knezevic, M., 2020. A comparative study between elasto-plastic self-consistent crystal plasticity and anisotropic yield function with distortional hardening formulations for sheet metal forming. Mech. Mater. 148, 103422.
Fleck, N.A., Muller, G.M., Ashby, M.F., Hutchinson, J.W., 1994. Strain gradient plasticity: theory and experiment. Acta Metall. Mater. 42, 475–487.
Fromm, B.S., Adams, B.L., Ahmadi, S., Knezevic, M., 2009. Grain size and orientation distributions: application to yielding of α-titanium. Acta Mater. 57, 2339–2348.
Gardey, B., Bouvier, S., Bacroix, B., 2005. Correlation between the macroscopic behavior and the microstructural evolutions during large plastic deformation of a dual-phase steel. Metall. Mater. Trans. 36, 2937–2945.
Ghaei, A., Green, D.E., Aryanpour, A., 2015. Springback simulation of advanced high strength steels considering nonlinear elastic unloading–reloading behavior. Mater. Des. 88, 461–470.
Ghorbanpour, S., Alam, M.E., Ferreri, N.C., Kumar, A., McWilliams, B.A., Vogel, S.C., Bicknell, J., Beyerlein, I.J., Knezevic, M., 2020. Experimental characterization and crystal plasticity modeling of anisotropy, tension-compression asymmetry, and texture evolution of additively manufactured Inconel 718 at room and elevated temperatures. Int. J. Plast. 125, 63–79.
Ghorbanpour, S., Zecevic, M., Kumar, A., Jahedi, M., Bicknell, J., Jorgensen, L., Beyerlein, I.J., Knezevic, M., 2017. A crystal plasticity model incorporating the effects of precipitates in superalloys: application to tensile, compressive, and cyclic deformation of Inconel 718. Int. J. Plast. 99, 162–185.
Goh, C.-H., Neu, R.W., McDowell, D.L., 2003. Crystallographic plasticity in fretting of Ti–6AL–4V. Int. J. Plast. 19, 1627–1650.
Gong, H., Wang, S., Knysh, P., Korkolis, Y.P., 2016. Experimental investigation of the mechanical response of laser-welded dissimilar blanks from advanced- and ultra-high-strength steels. Mater. Des. 90, 1115–1123.
Gough, H., Hanson, D., Wright, S., 1927. The behaviour of single crystals of aluminium under static and repeated stresses. In: Series A, Containing Papers of a Mathematical or Physical Character. Philosophical Transactions of the Royal Society of London, pp. 1–30.
Gracio, J.J., Barlat, F., Rauch, E.F., Jones, P.T., Neto, V.F., Lopes, A.B., 2004. Artificial aging and shear deformation behaviour of 6022 aluminium alloy. Int. J. Plast. 20, 427–445.
Harder, J., 1999. A crystallographic model for the study of local deformation processes in polycrystals. Int. J. Plast. 15, 605–624.
Hasegawa, T., Yakou, T., Karashima, S., 1975. Deformation behaviour and dislocation structures upon stress reversal in polycrystalline aluminium. Mater. Sci. Eng. 20, 267–276.
Holscher, M., Raabe, D., Lucke, K., 1994. Relationship between rolling textures and shear textures in F.C.C. and B.C.C. metals. Acta Metall. Mater. 42, 879–886.
Hosford, W.F., Caddell, R.M., 1993. Metal Forming Mechanics and Metallurgy. Prentice-Hall, Inc.
Hu, Z., Rauch, E.F., Teodosiu, C., 1992. Work-hardening behavior of mild steel under stress reversal at large strains. Int. J. Plast. 8, 839–856.
Jahedi, M., Ardeljan, M., Beyerlein, I.J., Paydar, M.H., Knezevic, M., 2015a. Enhancement of orientation gradients during simple shear deformation by application of simple compression. J. Appl. Phys. 117, 214309.
Jahedi, M., Ardjmand, E., Knezevic, M., 2017a. Microstructure metrics for quantitative assessment of particle size and dispersion: application to metal-matrix composites. Powder Technol 311, 226–238.
Jahedi, M., Beyerlein, I.J., Paydar, M.H., Zheng, S., Xiong, T., Knezevic, M., 2017b. Effects of pressure and number of turns on microstructural homogeneity developed in high-pressure double torsion. Metall. Mater. Trans. 48, 1249–1263.
Jahedi, M., Knezevic, M., Paydar, M., 2015b. High-pressure double torsion as a severe plastic deformation process: experimental procedure and finite element modeling. J. Mater. Eng. Perform. 24, 1471–1482.
Jahedi, M., Paydar, M.H., Knezevic, M., 2015c. Enhanced microstructural homogeneity in metal-matrix composites developed under high-pressure-double-torsion. Mater. Char. 104, 92–100.
Jahedi, M., Paydar, M.H., Zheng, S., Beyerlein, I.J., Knezevic, M., 2014. Texture evolution and enhanced grain refinement under high-pressure-double-torsion. Mater. Sci. Eng., A 611, 29–36.
Kadkhodapour, J., Schmauder, S., Raabe, D., Ziaei-Rad, S., Weber, U., Calcagnotto, M., 2011. Experimental and numerical study on geometrically necessary dislocations and non-homogeneous mechanical properties of the ferrite phase in dual phase steels. Acta Mater. 59, 4387–4394.
Kalidindi, S.R., Bronkhorst, C.A., Anand, L., 1992. Crystallographic texture evolution in bulk deformation processing of FCC metals. J. Mech. Phys. Solid. 40, 537–569.
Kapp, M., Hebesberger, T., Kolednik, O., 2011. A micro-level strain analysis of a high-strength dual-phase steel. Int. J. Mater. Res. 102, 687–691.
Kassner, M.E., Geantil, P., Levine, L.E., 2013. Long range internal stresses in single-phase crystalline materials. Int. J. Plast. 45, 44–60.
Kitayama, K., Tomé, C.N., Rauch, E.F., Gracio, J.J., Barlat, F., 2013. A Crystallographic Dislocation Model for Describing Hardening of Polycrystals during Strain Path Changes. Application to Low Carbon Steels. International Journal of Plasticity in press.
Knezevic, M., Al-Harbi, H.F., Kalidindi, S.R., 2009. Crystal plasticity simulations using discrete Fourier transforms. Acta Mater. 57, 1777–1784.
Knezevic, M., Beyerlein, I.J., Brown, D.W., Sisneros, T.A., Tomé, C.N., 2013a. A polycrystal plasticity model for predicting mechanical response and texture evolution during strain-path changes: application to beryllium. Int. J. Plast. 49, 185–198.
Knezevic, M., Capolungo, L., Tomé, C.N., Lebensohn, R.A., Alexander, D.J., Mihaila, B., McCabe, R.J., 2012. Anisotropic stress-strain response and microstructure evolution of textured α-uranium. Acta Mater. 60, 702–715.
Knezevic, M., Drach, B., Ardeljan, M., Beyerlein, I.J., 2014a. Three dimensional predictions of grain scale plasticity and grain boundaries using crystal plasticity finite element models. Comput. Methods Appl. Mech. Eng. 277, 239–259.
Knezevic, M., Kalidindi, S.R., 2007. Fast computation of first-order elastic-plastic closures for polycrystalline cubic-orthorhombic microstructures. Comput. Mater. Sci. 39, 643–648.
Knezevic, M., Kalidindi, S.R., 2017. Crystal plasticity modeling of microstructure evolution and mechanical fields during processing of metals using spectral databases. JOM 69, 830–838.
Knezevic, M., Kalidindi, S.R., Fullwood, D., 2008. Computationally efficient database and spectral interpolation for fully plastic Taylor-type crystal plasticity calculations of face-centered cubic polycrystals. Int. J. Plast. 24, 1264–1276.
Knezevic, M., Landry, N.W., 2015. Procedures for reducing large datasets of crystal orientations using generalized spherical harmonics. Mech. Mater. 88, 73–86.
Knezevic, M., Levinson, A., Harris, R., Mishra, R.K., Doherty, R.D., Kalidindi, S.R., 2010. Deformation twinning in AZ31: influence on strain hardening and texture evolution. Acta Mater. 58, 6230–6242.
Knezevic, M., McCabe, R.J., Lebensohn, R.A., Tomé, C.N., Liu, C., Lovato, M.L., Mihaila, B., 2013b. Integration of self-consistent polycrystal plasticity with dislocation density based hardening laws within an implicit finite element framework: application to low-symmetry metals. J. Mech. Phys. Solid. 61, 2034–2046.
Knezevic, M., McCabe, R.J., Tomé, C.N., Lebensohn, R.A., Chen, S.R., Cady, C.M., Gray Iii, G.T., Mihaila, B., 2013c. Modeling mechanical response and texture evolution of α-uranium as a function of strain rate and temperature using polycrystal plasticity. Int. J. Plast. 43, 70–84.
Knezevic, M., Nizolek, T., Ardeljan, M., Beyerlein, I.J., Mara, N.A., Pollock, T.M., 2014b. Texture evolution in two-phase Zr/Nb lamellar composites during accumulative roll bonding. Int. J. Plast. 57, 16–28.
Knezevic, M., Savage, D.J., 2014. A high-performance computational framework for fast crystal plasticity simulations. Comput. Mater. Sci. 83, 101–106.
Knezevic, M., Zecevic, M., Beyerlein, I.J., Lebensohn, R.A., 2016. A numerical procedure enabling accurate descriptions of strain rate-sensitive flow of polycrystals within crystal visco-plasticity theory. Comput. Methods Appl. Mech. Eng. 308, 468–482.
Kocks, U.F., Mecking, H., 1981. Kinetics of flow and strain-hardening. Acta Metall 29, 1865–1875.
Kocks, U.F., Tomé, C.N., Wenk, H.-R., 1998. Texture and Anisotropy. Cambridge University Press, Cambridge, UK.
Kruml, T., Coddet, O., Martin, J., 2008. About the determination of the thermal and athermal stress components from stress-relaxation experiments. Acta Mater. 56, 333–340.

Kudzal, A.D., McWilliams, B.A., Taggart-Scarff, J., Knezevic, M., 2020. Fabrication of a low alloy ultra-high strength (>1500 MPa yield) steel using powder bed fusion additive manufacturing. Mater. Sci. Eng., A 770, 138512.
Kuwabara, T., Kumano, Y., Ziegelheim, J., Kurosaki, I., 2009. Tension–compression asymmetry of phosphor bronze for electronic parts and its effect on bending behavior. Int. J. Plast. 25, 1759–1776.
Kuwabara, T., Nagata, K., Nakako, T., 2001. Measurement and analysis of the Bauschinger effect of sheet metals subjected to in plane stress reversals. Proceedings of AMPT 1, 407–412.
Lebensohn, R.A., Kanjarla, A.K., Eisenlohr, P., 2012. An elasto-viscoplastic formulation based on fast Fourier transforms for the prediction of micromechanical fields in polycrystalline materials. Int. J. Plast. 32–33, 59–69.
Lebensohn, R.A., Tomé, C.N., 1993. A self-consistent anisotropic approach for the simulation of plastic deformation and texture development of polycrystals: application to zirconium alloys. Acta Metall. Mater. 41, 2611–2624.
Lebensohn, R.A., Zecevic, M., Knezevic, M., McCabe, R.J., 2016. Average intragranular misorientation trends in polycrystalline materials predicted by a viscoplastic self-consistent approach. Acta Mater. 104, 228–236.
Lentz, M., Klaus, M., Beyerlein, I.J., Zecevic, M., Reimers, W., Knezevic, M., 2015a. In situ X-ray diffraction and crystal plasticity modeling of the deformation behavior of extruded Mg–Li–(Al) alloys: an uncommon tension–compression asymmetry. Acta Mater. 86, 254–268.
Lentz, M., Klaus, M., Wagner, M., Fahrenson, C., Beyerlein, I.J., Zecevic, M., Reimers, W., Knezevic, M., 2015b. Effect of age hardening on the deformation behavior of an Mg–Y–Nd alloy: in-situ X-ray diffraction and crystal plasticity modeling. Mater. Sci. Eng., A 628, 396–409.
Li, K., Carden, W., Wagoner, R., 2002. Simulation of springback. Int. J. Mech. Sci. 44, 103–122.
Li, L., Shen, L., Proust, G., 2014. A texture-based representative volume element crystal plasticity model for predicting Bauschinger effect during cyclic loading. Mater. Sci. Eng., A 608, 174–183.
Ma, A., Roters, F., Raabe, D., 2006a. A dislocation density based constitutive model for crystal plasticity FEM including geometrically necessary dislocations. Acta Mater. 54, 2169–2179.
Ma, A., Roters, F., Raabe, D., 2006b. On the consideration of interactions between dislocations and grain boundaries in crystal plasticity finite element modeling – theory, experiments, and simulations. Acta Mater. 54, 2181–2194.
Ma, A., Roters, F., Raabe, D., 2007. A dislocation density based constitutive law for BCC materials in crystal plasticity FEM. Comput. Mater. Sci. 39, 91–95.
Ma, B., Liu, Z.G., Jiang, Z., Wu, X., Diao, K., Wan, M., 2016. Prediction of forming limit in DP590 steel sheet forming: an extended fracture criterion. Mater. Des. 96, 401–408.
Madec, R., Devincre, B., Kubin, L., Hoc, T., Rodney, D., 2003. The role of collinear interaction in dislocation-induced hardening. Science 301, 1879–1882.
McDowell, D.L., 1992. A nonlinear kinematic hardening theory for cyclic thermoplasticity and thermoviscoplasticity. Int. J. Plast. 8, 695–728.
Mohebbi, M.S., Akbarzadeh, A., Yoon, Y.-O., Kim, S.-K., 2015. Stress relaxation and flow behavior of ultrafine grained AA 1050. Mech. Mater. 89, 23–34.
Mompiou, F., Caillard, D., Legros, M., Mughrabi, H., 2012. In situ TEM observations of reverse dislocation motion upon unloading in tensile-deformed UFG aluminium. Acta Mater. 60, 3402–3414.
Mughrabi, H., 1983. Dislocation wall and cell structures and long-range internal stresses in deformed metal crystals. Acta Metall 31, 1367–1379.
Mughrabi, H., 2001. On the role of strain gradients and long-range internal stresses in the composite model of crystal plasticity. Mater. Sci. Eng., A 317, 171–180.
Nesterova, E.V., Bouvier, S., Bacroix, B., 2015. Microstructure evolution and mechanical behavior of a high strength dual-phase steel under monotonic loading. Mater. Char. 100, 152–162.
Nieh, T.G., Nix, W.D., 1986. Unloading yield effects in aluminum alloys. Metallurgical transactions. A, Physical metallurgy and materials science 17 A, 121–126.
Nikhare, C., Hodgson, P., Weiss, M., 2011. Necking and fracture of advanced high strength steels. Mater. Sci. Eng., A 528, 3010–3013.
Ohno, N., 1982. A constitutive model of cyclic plasticity with a nonhardening strain region. J. Appl. Mech. 49 (4), 721–727.
Ohno, N., Kachi, Y., 1986. A constitutive model of cyclic plasticity for nonlinear hardening materials. J. Appl. Mech. 53 (2), 395–403.
Orowan, E., 1959. In: Rassweiler, G.M., Grube, W.L. (Eds.), Causes and Effects of Internal Stresses, General Motors Symposium. Elsevier, Amsterdam, pp. 59–80.
Pavlina, E., Lee, M.-G., Barlat, F., 2015. Observations on the nonlinear unloading behavior of advanced high strength steels. Metall. Mater. Trans. 46, 18–22.
Poulin, C.M., Vogel, S.C., Korkolis, Y.P., Kinsey, B.L., Knezevic, M., 2020. Experimental studies into the role of cyclic bending during stretching of dual-phase steel sheets. Int. J. Material Form. 13, 393–408.
Prasad, K., Krishnaswamy, H., Arunachalam, N., 2020. Investigations on ductility improvement and reloading yielding during stress relaxation of dual phase Ti–6Al–4V titanium alloy. J. Alloys Compd. 828, 154450.
Rauch, E.F., Gracio, J.J., Barlat, F., 2007. Work-hardening model for polycrystalline metals under strain reversal at large strains. Acta Mater. 55, 2939–2948.
Risse, M., Lentz, M., Fahrenson, C., Reimers, W., Knezevic, M., Beyerlein, I.J., 2017. Elevated temperature effects on the plastic anisotropy of an extruded Mg-4 Wt pct Li alloy: experiments and polycrystal modeling. Metall. Mater. Trans. 48, 446–458.
Roemer, T.J., Barrett, T.J., Knezevic, M., Kinsey, B.L., Korkolis, Y.P., 2019. Experimental study of continuous-bending-under-tension of AA6022-T4. J. Mater. Process. Technol. 266, 707–714.
Saeidi, N., Ashrafizadeh, F., Niroumand, B., Barlat, F., 2015. EBSD study of micromechanisms involved in high deformation ability of DP steels. Mater. Des. 87, 130–137.
Savage, D.J., Chandola, N., Cazacu, O., McWilliams, B.A., Knezevic, M., 2018. Validation of recent analytical dilatational models for porous polycrystals using crystal plasticity finite element models with Schmid and non-Schmid activation laws. Mech. Mater. 126, 148–162.
Savage, D.J., Feng, Z., Knezevic, M., 2021a. Identification of crystal plasticity model parameters by multi-objective optimization integrating microstructural evolution and mechanical data. Comput. Methods Appl. Mech. Eng. 379, 113747.
Savage, D.J., Knezevic, M., 2015. Computer implementations of iterative and non-iterative crystal plasticity solvers on high performance graphics hardware. Comput. Mech. 56, 677–690.
Savage, D.J., McCabe, R.J., Knezevic, M., 2021b. An automated procedure built on MTEX for reconstructing deformation twin hierarchies from electron backscattered diffraction datasets of heavily twinned microstructures. Mater. Char. 171, 110808.
Segurado, J., Lebensohn, R.A., Llorca, J., Tomé, C.N., 2012. Multiscale modeling of plasticity based on embedding the viscoplastic self-consistent formulation in implicit finite elements. Int. J. Plast. 28, 124–140.
Sharma, R., Poulin, C.M., Knezevic, M., Miles, M.P., Fullwood, D.T., 2021. Micromechanical origins of remarkable elongation-to-fracture in AHSS TRIP steels via continuous bending under tension. Mater. Sci. Eng., A 825, 141876.
Shi, M., Gelisse, S., 2006. Issues on the AHSS forming limit determination. In: Proceedings of the IDDRG International Conference, pp. 19–21. Porto, Portugal.
Smith, A., Chen, Z., Lee, J.Y., Lee, M.G., Wagoner, R.H., 2014. Effective method for fitting complex constitutive equations. Int. J. Plast. 58, 100–119.
Sritharan, T., Chandel, R.S., 1997. Phenomena in interrupted tensile tests of heat treated aluminium alloy 6061. Acta Mater. 45, 3155–3161.
Stout, M., Rollett, A., 1990. Large-strain Bauschinger effects in fcc metals and alloys. Metall. Mater. Trans. 21, 3201–3213.
Tasan, C.C., Hoefnagels, J.P.M., Diehl, M., Yan, D., Roters, F., Raabe, D., 2014. Strain localization and damage in dual phase steels investigated by coupled in-situ deformation experiments and crystal plasticity simulations. Int. J. Plast. 63, 198–210.
Taupin, V., Pesci, R., Berbenni, S., Berveiller, S., Ouahab, R., Bouaziz, O., 2013. Lattice strain measurements using synchrotron diffraction to calibrate a micromechanical modeling in a ferrite–cementite steel. Mater. Sci. Eng., A 561, 67–77.
Taylor, G., 1992. Thermally-activated deformation of BCC metals and alloys. Prog. Mater. Sci. 36, 29–61.
Taylor, G.I., 1938. Plastic strain in metals. J. Inst. Met. 62, 307–324.
Turner, P.A., Tomé, C.N., 1994. A study of residual stresses in Zircaloy-2 with rod texture. Acta Metall. Mater. 42, 4143–4153.
Verma, R.K., Kuwabara, T., Chung, K., Haldar, A., 2011. Experimental evaluation and constitutive modeling of non-proportional deformation for asymmetric steels. Int. J. Plast. 27, 82–101.
Wagoner, R.H., Kim, J.H., Sung, J.H., 2009. Formability of advanced high strength steels. Int. J. Material Form. 2, 359.
Wagoner, R.H., Lim, H., Lee, M.-G., 2013. Advanced issues in springback. Int. J. Plast. 45, 3–20.
Wen, W., Borodachenkova, M., Tomé, C.N., Vincze, G., Rauch, E.F., Barlat, F., Grácio, J. J., 2015. Mechanical behavior of Mg subjected to strain path changes: experiments and modeling. Int. J. Plast. 73, 171–183.
Wenk, H.-R., Lutterotti, L., Vogel, S., 2003. Texture analysis with the new HIPPO TOF diffractometer. Nucl. Instrum. Methods Phys. Res. Sect. A Accel. Spectrom. Detect. Assoc. Equip. 515, 575–588.
Wenk, H.-R., Lutterotti, L., Vogel, S., 2010. Rietveld texture analysis from TOF neutron diffraction data. Powder Diffr. 25, 283–296.
Wilson, D.V., Bate, P.S., 1986. Reversibility in the work hardening of spheroidised steels. Acta Metall 34, 1107–1120.
Wilson, D.V., Zandrahimi, M., Roberts, W.T., 1990. Effects of changes in strain path on work-hardening in CP aluminium and an Al-Cu-Mg alloy. Acta Metall. Mater. 38, 215–226.
Wollmershauser, J.A., Clausen, B., Agnew, S.R., 2012. A slip system-based kinematic hardening model application to in situ neutron diffraction of cyclic deformation of austenitic stainless steel. Int. J. Fatig. 36, 181–193.
Woo, W., Em, V.T., Kim, E.Y., Han, S.H., Han, Y.S., Choi, S.H., 2012. Stress–strain relationship between ferrite and martensite in a dual-phase steel studied by in situ neutron diffraction and crystal plasticity theories. Acta Mater. 60, 6972–6981.
Xu, B., Jiang, Y., 2004. A cyclic plasticity model for single crystals. Int. J. Plast. 20, 2161–2178.
Xue, X., Liao, J., Vincze, G., Sousa, J., Barlat, F., Gracio, J., 2016. Modelling and sensitivity analysis of twist springback in deep drawing of dual-phase steel. Mater. Des. 90, 204–217.
Yaddanapudi, K., Knezevic, M., Mahajan, S., Beyerlein, I.J., 2021. Plasticity and structure evolution of ferrite and martensite in DP 1180 during tension and cyclic bending under tension to large strains. Mater. Sci. Eng., A 820, 141536.
Yoshida, F., Uemori, T., Fujiwara, K., 2002. Elastic–plastic behavior of steel sheets under in-plane cyclic tension–compression at large strain. Int. J. Plast. 18, 633–659.
Zang, S.-l., Lee, M.-g., Hoon Kim, J., 2013. Evaluating the significance of hardening behavior and unloading modulus under strain reversal in sheet springback prediction. Int. J. Mech. Sci. 77, 194–204.
Zecevic, M., Beyerlein, I.J., Knezevic, M., 2017a. Coupling elasto-plastic self-consistent crystal plasticity and implicit finite elements: applications to compression, cyclic tension-compression, and bending to large strains. Int. J. Plast. 93, 187–211.
Zecevic, M., Knezevic, M., 2015. A dislocation density based elasto-plastic self-consistent model for the prediction of cyclic deformation: application to Al6022-T4. Int. J. Plast. 72, 200–217.

Zecevic, M., Knezevic, M., 2017. Modeling of sheet metal forming based on implicit embedding of the elasto-plastic self-consistent formulation in shell elements: application to cup drawing of AA6022-T4. JOM 69, 922–929.
Zecevic, M., Knezevic, M., 2018a. Latent hardening within the elasto-plastic self-consistent polycrystal homogenization to enable the prediction of anisotropy of AA6022-T4 sheets. Int. J. Plast. 105, 141–163.
Zecevic, M., Knezevic, M., 2018b. A new visco-plastic self-consistent formulation implicit in dislocation-based hardening within implicit finite elements: application to high strain rate and impact deformation of tantalum. Comput. Methods Appl. Mech. Eng. 341, 888–916.
Zecevic, M., Knezevic, M., 2019. An implicit formulation of the elasto-plastic self-consistent polycrystal plasticity model and its implementation in implicit finite elements. Mech. Mater. 136, 103065.
Zecevic, M., Knezevic, M., Beyerlein, I.J., McCabe, R.J., 2016a. Origin of texture development in orthorhombic uranium. Mater. Sci. Eng., A 665, 108–124.
Zecevic, M., Knezevic, M., McWilliams, B., Lebensohn, R.A., 2020. Modeling of the thermo-mechanical response and texture evolution of WE43 Mg alloy in the dynamic recrystallization regime using a viscoplastic self-consistent formulation. Int. J. Plast. 130, 102705.
Zecevic, M., Korkolis, Y.P., Kuwabara, T., Knezevic, M., 2016b. Dual-phase steel sheets under cyclic tension–compression to large strains: experiments and crystal plasticity modeling. J. Mech. Phys. Solid. 96, 65–87.
Zecevic, M., Lebensohn, R.A., McCabe, R.J., Knezevic, M., 2018. Modeling of intragranular misorientation and grain fragmentation in polycrystalline materials using the viscoplastic self-consistent formulation. Int. J. Plast. 109, 193–211.
Zecevic, M., Lebensohn, R.A., McCabe, R.J., Knezevic, M., 2019a. Modelling recrystallization textures driven by intragranular fluctuations implemented in the viscoplastic self-consistent formulation. Acta Mater. 164, 530–546.
Zecevic, M., McCabe, R.J., Knezevic, M., 2015a. A new implementation of the spectral crystal plasticity framework in implicit finite elements. Mech. Mater. 84, 114–126.
Zecevic, M., McCabe, R.J., Knezevic, M., 2015b. Spectral database solutions to elasto-viscoplasticity within finite elements: application to a cobalt-based FCC superalloy. Int. J. Plast. 70, 151–165.
Zecevic, M., Pantleon, W., Lebensohn, R.A., McCabe, R.J., Knezevic, M., 2017b. Predicting intragranular misorientation distributions in polycrystalline metals using the viscoplastic self-consistent formulation. Acta Mater. 140, 398–410.
Zecevic, M., Upadhyay, M.V., Polatidis, E., Panzner, T., Van Swygenhoven, H., Knezevic, M., 2019b. A crystallographic extension to the Olson-Cohen model for predicting strain path dependence of martensitic transformation. Acta Mater. 166, 386–401.